Materials Science & Engineering A 872 (2023) 144946

Contents lists available at ScienceDirect

Materials Science & Engineering A

journal homepage: www.elsevier.com/locate/msea

Deformation behavior and strengthening effects of an eutectic $AlCoCrFeNi_{2.1}$ high entropy alloy probed by in-situ synchrotron X-ray diffraction and post-mortem EBSD

Jiajia Shen [a,**], J.G. Lopes [a], Zhi Zeng [b], Yeon Taek Choi [c], E. Maawad [d], N. Schell [d], Hyoung Seop Kim [c,h], Rajiv S. Mishra [e,f], J.P. Oliveira [g,*]

[a] UNIDEMI, Department of Mechanical and Industrial Engineering, NOVA School of Science and Technology, Universidade NOVA de Lisboa, Caparica, 2829-516, Portugal
[b] School of Mechanical and Electrical Engineering, University of Electronic Science and Technology of China, Sichuan, 611731, China
[c] Graduate Institute of Ferrous Technology, POSTECH (Pohang University of Science and Technology), Pohang, 790-794, South Korea
[d] Institute of Materials Physics, Helmholtz-Zentrum Hereon, Max-Planck-Str. 1, Geesthacht, D-21502, Germany
[e] Department of Materials Science and Engineering, University of North Texas, Denton, TX, 76207, USA
[f] Center for Agile and Adaptive Additive Manufacturing (CAAAM), University of North Texas, Denton, TX, 76207, USA
[g] CENIMAT|i3N, Department of Materials Science, School of Science and Technology, NOVA University Lisbon, Caparica, Portugal
[h] Institute for Convergence Research and Education in Advanced Technology, Yonsei University, Seoul, 03722, South Korea

ARTICLE INFO

Keywords:
High entropy alloys
Synchrotron X-ray diffraction
In-situ testing
Strengthening mechanisms

ABSTRACT

In this work, high energy synchrotron X-ray diffraction was used during tensile testing of an as-cast eutectic $AlCoCrFeNi_{2.1}$ high entropy alloy. Aside, from determining for the first time the volume fractions of existing phases, we further detail their role on the alloy deformation behavior. The two major phases, a soft disordered FCC and a hard ordered B2 BCC, were observed to exhibit a stress partitioning effect which can be used to modulate the mechanical response of the material based on the relative volume fraction of each phase. Dislocation density analysis revealed that the soft FCC phase had a significantly higher dislocation density right after the onset of plastic deformation. This is attributed to the existence of strain gradients across the lamellar structure, where the hard B2 BCC prevents free deformation of the FCC phase. Nonetheless, despite the increase of the dislocation density in the soft FCC phase, calculations of the strengthening effects induced by generation of dislocations are more significant in the hard B2 BCC phases, as this phase is primarily responsible for the strength increase in the alloy. Besides, the evolutions in dislocation density of the soft FCC and hard B2 BCC phases during tensile deformation obtained from synchrotron X-ray diffraction data are consistent with the evolution of KAM determined by EBSD characterization. Also, lattice strain analysis across two principal directions (parallel and perpendicular to the loading axis) reveals that for these specific orientations there is a preferential deformation of the hard FCC planes which can be related to the deformation response of specific lattice planes at distinct orientations, as well as to the phase partitioning stress behavior.

1. Introduction

High entropy alloys (HEAs), also known as multi-principal alloys, have attracted widespread interest in the field of materials science for their good thermal stability [1,2], high ductility and strength [3–6], and excellent corrosion resistance [7–9], since they were first proposed by Yeh et al. [10] and Cantor et al. [11] in 2004. Specific examples of alloy systems that possess remarkable properties include the Ti–Zr–Nb–Al with a good strength/ductility balance [12], the Nb–Ta–Ti–V–Zr for ultra-high strength applications [3], and the Al–Co–Cr–Cu–Fe–Ni for improved corrosion resistance [13]. Despite their complex compositions, containing typically at least five principal elements [14], HEAs often exhibit simple crystal structures, with face-centered cubic (FCC) and body-centered cubic (BCC) being the most prevalent ones.

* Corresponding author.
** Corresponding author.
E-mail addresses: j.shen@campus.fct.unl.pt (J. Shen), jp.oliveira@fct.unl.pt (J.P. Oliveira).

https://doi.org/10.1016/j.msea.2023.144946
Received 1 January 2023; Received in revised form 21 March 2023; Accepted 24 March 2023
Available online 27 March 2023

For single-phase HEAs with FCC structure, such as the equiatomic CoCrFeMnNi [15], $Fe_{40}Mn_{26}Ni_{27}Co_5Cr_2$ [16], and $Fe_{40}Mn_{40}Co_{10}Cr_{10}$ [17], the yield strength is almost always below 400 MPa (except if previous plastic deformation has been applied), although they reach elongations of more than 50%. For single BCC HEAs compositions, such as equiatomic NbMoTaW and VNbMoTaW [1], the yield strength can be above 1000 MPa, but the alloy elongation is significantly reduced as compared to single FCC HEAs. In addition, the casting properties and compositional segregation of HEAs can further limit their practical applications [18,19].

One of the most sought-after challenges in metallurgical research concerns the ability to develop alloys with a good balance of strength and elongation. This trade-off seems to be absent in single-phase HEAs [20,21]. In order to solve this challenge and achieve simultaneous high strength and ductility, Lu et al. first proposed the concept of eutectic HEAs [22]. In their seminal work, an $AlCoCrFeNi_{2.1}$ HEA consisting of soft and hard phases within a lamellar microstructure was developed. Subsequently, other eutectic HEAs, such as $Fe_{20}Co_{20}Ni_{41}Al_{19}$ [23], $AlCrFeNiMo_{0.2}$ [24], and $Nb_{25}Sc_{25}Ti_{25}Zr_{25}$ [25], have emerged. However, among all currently available eutectic HEAs, the most studied is still the $AlCoCrFeNi_{2.1}$ composition. Of special relevance in this composition are its good thermophysical properties, including reduced solidification temperature range arising from the isothermal transition of the eutectic reaction of the alloy in its as-cast condition [24].

The potential for as-cast $AlCoCrFeNi_{2.1}$ eutectic HEAs as engineering materials for structural application has been studied by different research groups primarily focusing on two main aspects: the effect of thermomechanical treatments on the microstructure evolution and resulting properties [26–33]; dependence of the mechanical properties under service conditions [34–40]. In 2016, Wani et al. [41] performed for the first time thermomechanical processing on the $AlCoCrFeNi_{2.1}$ alloy, which included significant cold-rolling followed by multiple annealing treatments. It was shown, by electron microscopy characterization, that the as-cast microstructure was composed of a lamellar B2 BCC + $L1_2$ FCC microstructure. After thermomechanical processing, the ordered $L1_2$ become disordered, whereas no microstructural changes in the B2 BCC phase were observed. Bhattacharjee et al. [34] investigated the effect of low-temperature tensile testing (from room temperature to 77 K) on the mechanical properties of an as-cast $AlCoCrFeNi_{2.1}$ alloy. Again, disordering of the $L1_2$ phase and subsequent transformation to a simple FCC phase was reported, whereas the B2 BCC phase remained unchanged. Moreover, the fracture strains were seen to be practically constant with decreasing testing temperature, while the tensile strength increased by ≈ 300 MPa. Zhang et al. [39] performed high-temperature tensile tests on an as-cast $AlCoCrFeNi_{2.1}$ eutectic HEA composed of $L1_2$ FCC and B2 BCC phases, which exhibited good strength and high plasticity at high temperatures due to the simultaneous hardening and dynamic recrystallization during deformation. In addition to this, Guo et al. [37] studied, in-situ, the deformation response of a similar alloy over a wide temperature range (from 77 to 676 K) using neutron diffraction, highlighting the microstructural evolution of both phases. Finally, Lu et al. [42] investigated the mechanical behavior and microstructural evolution of both FCC and B2 BCC phases at room and cryogenic temperatures, and detected that no phase transformation occurred until fracture, revealing that combination of high strength and ductility does not originate from a stress-induced phase transformation.

It is worth noting that phase identification of the as-cast eutectic $AlCoCrFeNi_{2.1}$ HEA is predominantly performed by transmission electron microscopy (TEM). Moreover, several researchers have identified different phases in the as-cast $AlCoCrFeNi_{2.1}$ HEA. Some authors have identified disordered FCC and ordered B2 BCC phases [32,43–46], others have identified ordered $L1_2$ FCC and B2 BCC phases [37,47–52], while some have simultaneously identified FCC, $L1_2$ FCC, B2 BCC, and tetragonal σ phases [53]. Additionally, studies on the as-cast $AlCoCrFeNi_{2.1}$ eutectic HEA have been primarily focused on qualitatively exploring the mechanical properties of the alloy under different deformation conditions (e.g., low temperature [27,29,34,37] vs room [37,38,54] vs high temperature [22,31,37,39,41,47,49,52], and fatigue [55]). A comprehensive quantitative study of the deformation mechanisms of the different phases that exist in this alloy and their impact on the macroscopic mechanical response is yet lacking, thus hampering a full understanding of microstructure/properties relationships.

In this work, we use in-situ high-energy synchrotron X-ray diffraction to evaluate the micromechanical behavior and microstructure evolution of an as-cast $AlCoCrFeNi_{2.1}$ eutectic HEA during tensile deformation until failure. Aside from quantifying for the first time all phases that coexist in the material, the contribution of each phase towards the mechanical strength of the alloy is determined and rationalized not only based on the dislocation density evolution but also on the impact of the lamellar structure. We also highlight the possibility to tune the strength/ductility response of eutectic HEAs by modifying the volume fractions of existing phases. Lattice strain measurements reveal the impact of the as-cast texture on the preferential deformation behavior of specific (h k l) planes.

2. Experimental procedures and methods

2.1. Starting material

Commercially pure Al, Co, Cr, Fe, Ni (99.9 wt% for Al, Co, and Ni and 99.5 wt% for Cr and Fe) were used to cast the $AlCoCrFeNi_{2.1}$ eutectic high entropy alloy by vacuum induced melting. The ingot was remelted multiple times to ensure good chemical homogeneity. The chemical composition of the material is detailed in Table 1. Since the eutectic $AlCoCrFeNi_{2.1}$ high entropy alloy possesses a good strength/ductility balance in the as-cast condition, the material was tested without the application of any heat treatments. Dog-bone-shaped tensile specimens were obtained using electrical discharge machining, and the material surfaces were polished with 2000-grit Silicon Carbide (SiC) prior to the in-situ synchrotron measurements. The gauge length, width, and thickness of the tensile specimens were 16, 1.2, and 1.5 mm, respectively.

Standard metallographic techniques were employed to obtain an overall view of the microstructural features of the as-cast material. The material was cold-mounted and ground using SiC papers with grit sizes varying from 300 to 4000, followed by polishing with a diamond paste suspension. It is worth mentioning that prior to etching, the samples were placed in an ultrasonic bath to remove any residual particles left from the SiC papers or the diamond suspension. Then, a solution of hydrochloric acid and nitric acid (3:1 in volume) was used to reveal the grain size and microstructural features of the eutectic alloy. The etching time was 15 s. A Leica DMI 5000 M inverted optical microscope was used to capture the abovementioned microstructural features.

In addition, Electron Backscatter Diffraction (EBSD) was performed on a Helios JSM-7100F to investigate the dynamic microstructure evolution along the tensile specimen.

2.2. In-situ synchrotron x-ray diffraction tensile experiments and analysis

To investigate the deformation behavior of the eutectic $AlCoCrFeNi_{2.1}$ high entropy alloy when subjected to uniaxial tensile testing at room temperature, in-situ high-energy synchrotron X-ray diffraction was performed at the P07 High Energy Materials Science beamline of Petra III/DESY (Hamburg, Germany). The experimental setup is depicted in Fig. 1. Dog-bone specimens were mounted on a laboratory-scale

Table 1
Nominal composition of the as-cast $AlCoCrFeNi_{2.1}$ high entropy alloy.

Chemical composition of as-cast $AlCoCrFeNi_{2.1}$ eutectic high entropy alloy [at%]					
Element	Al	Co	Cr	Fe	Ni
Composition	16.39	16.39	16.39	16.39	34.43

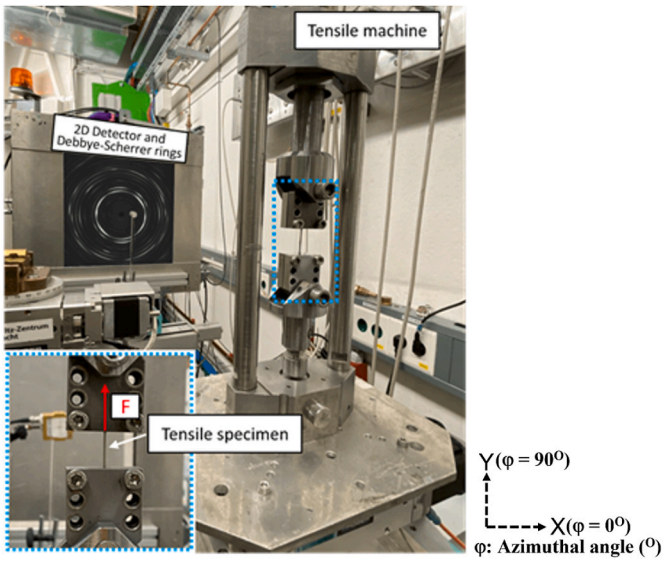

Fig. 1. High-energy in-situ synchrotron XRD experimental set-up. The Debbye-Scherrer rings shown in the image correspond to the analyzed sample.

Universal Testing Machine with a maximum load capacity of 20 kN. A high energy beam of 87 keV (corresponding to a wavelength of 0.14235 Å) was used. This energy allowed to work in transmission mode and capture bulk microstructure information. The beam size was 700 × 700 μm^2. The material was loaded to predefined strains to analyze both the elastic and plastic behaviors of the eutectic alloy. A PerkinElmer 2D detector with a pixel size of 200 × 200 μm^2 was used to capture the 2D raw Debbye-Scherrer rings at different stress/strain levels. The exposure time for each loading step was of 0.2 s and 10 images (including dark images for background subtraction) were obtained. The recorded dark images are subtracted from each image to significantly reduce any residuals coming from previous exposure. Prior to the in-situ testing, LaB_6 was used to determine the peak broadening associated with the beamline and its optics, as well as to determine the sample-to-detector distance (which was calculated to be 1226 mm).

To understand the orientation dependence of the microstructure evolution during tensile testing, the diffraction rings were caked into 24 parts, each corresponding to an azimuthal angle of 15°. According to the laboratorial reference (refer to Fig. 1), the azimuthal angle range from 82.5 to 97.5° was used to determine the microstructural evolution along the loading direction (LD), whereas the azimuthal range between −7.5 and 7.5° corresponded to the transverse direction (TD), i.e., perpendicular to the tensile loading axis. The caking procedure was performed using Fit2D software [56,57]. By integrating along specified azimuthal ranges, the two-dimensional Debye-Scherrer rings can be converted into a conventional one-dimensional intensity vs 2θ diffraction patterns. During tensile loading, no rotation of the sample was imposed, since the quantitative evolution of texture was outside the scope of this work.

The lattice strain and orientation-dependent elastic modulus for different (h k l) planes, as well as the dislocation density evolution and phase stress partitioning, were calculated as further detailed below. A pseudo-Voigt function was used for single peak fitting to determine key peak parameters such as peak position, peak intensity, and Full Width at Half Maximum (FWHM) using the General Structure Analysis System (GSASII) software [58]. In addition to this, the Material Analysis Using Diffraction (MAUD) [59,60] software was used to determine the volume fraction of existing phases via Rietveld refinement as well as for phase identification. The implemented Rietveld refinement routine used the Cagliott PV model consider the instrumental broadening [61], while for the anisotropic broadening the Popa model was used [62]. The extended Williams-Imhof-Matthies-Vinel (E-WIMV) algorithm [63] was used as the texture model. Finally, the material stress state was also considered by the implementation of a triaxial elastic stress model [59,64]. From the Rietveld refinement, the lattice parameters of the existing phases within the as-cast eutectic $AlCoCrFeNi_{2.1}$ high entropy alloy were also determined. LaB_6 powder was used as a defect-free standard specimen for calibration of the instrumental parameters.

Below we define how several microstructural features of interest were determined.

2.2.1. Lattice strain calculation

To study the evolution of the lattice strain during tensile loading along the LD and TD, individual reflections of the existing phases are fitted and the d-spacing at each loading step was obtained. Then, the lattice strain for a given (h k l) plane, ε_{hkl}, can be calculated according to Eq. (1) [65]:

$$\varepsilon_{hkl} = \frac{d_{hkl} - d_0}{d_{hkl}} \left(x10^6\right) \tag{1}$$

where (h k l) refers to a specific lattice plane, d_0 is the reference d-spacing before loading, neglecting any initial internal stresses [66], and d_{hkl} is the d-spacing determined at different stress/strain levels. The d_0 and d_{hkl} values can be obtained directly from the individual peak fitting procedure.

2.2.2. Phase stress calculation

To understand the mechanical behavior of the as-cast $AlCoCrFeNi_{2.1}$ eutectic high entropy alloy, the (3 1 1) FCC and (2 1 1) B2 BCC planes were chosen as the representative crystallographic planes to calculate the phase stress evolution. The (3 1 1) plane for an FCC structure and the (2 1 1) plane for a BCC structure are known to be the least affected by intergranular stresses (since grains with different orientations are subjected to different stress states), thus enabling the reliable calculation of the stress partitioning during tensile testing [67–69]. This has been demonstrated by numerical simulations as detailed in [70]. Based on the lattice strain evolution, the distribution of the applied load between both phases during deformation can be approximated. Thus, the Von Mises stress (σ_{vm}) is employed to quantify the phase stress partitioning during tensile deformation [68,69]. σ_{11} and σ_{22} are defined as below.

$$\sigma_{11} = \frac{E}{1+\upsilon}\varepsilon_{11} + \frac{\upsilon E}{(1+\upsilon)(1-2\upsilon)}(\varepsilon_{11} + \varepsilon_{22} + \varepsilon_{33}) \tag{2}$$

$$\sigma_{22} = \sigma_{33} = \frac{E}{1+\upsilon}\varepsilon_{22} + \frac{\upsilon E}{(1+\upsilon)(1-2\upsilon)}(\varepsilon_{11} + \varepsilon_{22} + \varepsilon_{33}) \tag{3}$$

$$\upsilon = -\frac{\varepsilon_{transverse}}{\varepsilon_{longitudianl}} \tag{4}$$

Here, ε_{11} is the lattice strain along the LD (obtained from the azimuthal range from 82.5 to 97.5°), ε_{22} is the lattice strain in the TD (obtained from the azimuthal range from −7.5° to 7.5°). ε_{33} is assumed to equal to ε_{22} [69,71]; ν is the Poisson ratio, which is known to vary within 0.35 and 0.39 for the as-cast $AlCoCrFeNi_{2.1}$ high entropy alloy studied in this work [37]; E is the orientation-dependent Young's modulus for a specific (h k l) plane, which can be obtained by fitting the evolution of the lattice strain during elastic deformation; σ_{11} is the principal stress in the loading direction, σ_{22} and σ_{33} are the principal stresses in the other two perpendicular directions. It is worth noting that, since the transverse stress (σ_{22}) is significantly smaller than the σ_{11} longitudinal stresses (with the sample applying for the σ_{33} stress, due to the reduced thickness of the material [72]), it is assumed here that $\sigma_{22} = \sigma_{33} \approx 0$ [68,73].

Next, the rule-of-mixtures (ROM) [74,75] was used to evaluate the strengthening effect of the B2 BCC phase as a function of different volume fraction contents.

$$\sigma = \nu_{\text{B2 BCC}} \times \sigma_{\text{B2 BCC}} + (1 - V_{\text{B2 BCC}}) \times \sigma_{\text{FCC}} \tag{5}$$

In this equation, $\nu_{B2\ BCC}$ corresponds to the volume fraction of B2 BCC phase, $\sigma_{B2\ BCC}$ and σ_{FCC} are the stresses imparted during the tensile process.

2.2.3. Dislocation density evolution

To evaluate the dislocation density during the room temperature tensile testing, the modified Williamson-Hall method [76,77] was used. The FWHM for a given (h k l) plane obtained from the individual peak fitting routine is mainly composed of three components: instrumental broadening, grain size broadening, and microstrain broadening, the latter resulting directly in the generation of defects such as dislocations and stacking faults [78]. After subtracting the instrumental peak broadening, the structural FWHM is mainly caused by grain size, $FWHM_{size}$, and microstrain, $FWHM_{microstrain}$ as shown in Eq. (6),

$$FWHM = \left[(FWHM_{measured})^2 - (FWHM_{instrumental})^2\right]^{1/2} \quad (6)$$

$$FWHM = FWHM_{size} + FWHM_{microstrain} \quad (7)$$

where,

$$FWHM_{size} = \frac{K\lambda}{L\cos\theta} \quad (8)$$

$$FWHM_{microstrain} = 4\varepsilon\frac{\sin\theta}{\cos\theta} \quad (9)$$

The FWHM induced by grain size ($FWHM_{size}$) and microstrain ($FWHM_{microstrain}$) are detailed in Eq. (8) and Eq. (9), respectively. Here, λ is the wavelength (0.14235 Å), L is the average grain size, k is the Scherrer constant (≈0.9) [79], and θ is half of the diffraction angle of the selected reflection.

Then, Eq. (10) is obtained by substituting Eqs. (8) and (9) into Eq. (7) and the average lattice strain, ε_0, and the crystallite size, L, are respectively the slope and line intercept of the linear relationship obtained when plotting FWHM x cos (θ) against 4 x sin (θ) for each of the selected diffraction peaks at different stress/strain levels [79–82]. In other words, for a linear equation of the y = mx + b type, FWHM x cos θ will correspond to y, 4 sin θ to x, ε_0 to k, and kλ/L to b.

$$FWHM\ x\ cos\ \theta = \frac{\kappa\lambda}{L} + 4\varepsilon_0\ \sin\theta \quad (10)$$

The dislocation density evolution of the two major phases of the eutectic alloy (disordered FCC and ordered B2 BCC) can be derived from the modified Williamson-Hall method as described by Eq. (11) [83],

$$\rho = \frac{\kappa{\varepsilon_0}^2}{b^2} \quad (11)$$

where ρ refers to the dislocation density, ε_0 corresponds to the lattice strain as defined above, and b is the Burgers vector, considering the {111}⟨110⟩ slip systems of the FCC phase and {110}⟨111⟩ slip systems of the B2 BCC phase [32]. The Burgers vectors of the FCC phase and B2 BCC phase can be estimated by using $b_{FCC} = \sqrt{2}a/2$ and $b_{B2\ BCC} = \sqrt{3}a/2$, respectively, where a is the corresponding lattice parameter, and k is a constant, with the values of k for the FCC and B2 BCC phases being 16.1 and 14.4, respectively [83].

After plastic deformation of the $AlCoCrFeNi_{2.1}$ alloy, dislocations are generated, move, and accumulate inside the material. This leads to the hardening behavior of the material upon plastic deformation. Therefore, in order to further understand the strength contribution resulting from the generation of new dislocations in both FCC and B2 BCC phases, the Bailey-Hirsch model was used as detailed by Eq. (12) [80],

$$\Delta\sigma_D = M\alpha Gb\rho^{1/2} \quad (12)$$

where $\Delta\sigma_D$ is the contribution due to the dislocations that are generated within each phase, M is the average Taylor factor, taking the values of 3.06 for the FCC phase and 2.8 for the B2 BCC phase based on EBSD data of the material studied in the current work, α is a constant, and the values for the FCC and B2 BCC phase are the same, being equal to 0.23 [67], G is the shear modulus for both matrix phases, with the FCC matrix phase having 76.9 GPa [84] and the B2 BCC phase possessing 80 GPa [85], b is the length of Burgers vector [86], and ρ is the dislocation density, which was calculated as detailed above. It should be mentioned that there are other strengthening mechanisms that can contribute to modifying the mechanical response of this eutectic high entropy alloy. These include solid solution, grain boundaries, and precipitates [80]. However, in this work, the only microstructural change occurring pertains to the dislocation density, while the other features were constant during deformation. For this reason, the mechanical behavior and strain-hardening behavior of the studied alloy have been primarily derived from the dislocation density evolution in both phases as it will be shown in the results and discussion section.

3. Results and discussion

3.1. Microstructural characterization and phase identification

Fig. 2 shows the microstructure of the $AlCoCrFeNi_{2.1}$ eutectic high-entropy alloy in the as-cast state, (a) before tensile deformation, (b) after the tensile test, and the fracture site occurred near the necking region as shown in Fig. 2 b). Previous reports in the literature [53] indicate that the microstructure corresponding to the bright (light contrast) and dark (dark contrast) corresponds to the FCC and B2 BCC phases, respectively. Macroscopic measurements of the average lamellae thickness distances reveal subtle changes before and after deformation. Prior to mechanical loading, the average lamellae thickness values of the FCC and B2 BCC phases were 2.41 ± 0.39 and 1.99 ± 0.34 μm, respectively, which then changes to 2.97 ± 0.41 and 2.40 ± 0.21 μm. This corresponds to a change of roughly 20–23% for each phase, suggesting that the overall deformation is homogenous. The reason for this is related to the distinct mechanical behavior of both phases and to constraint effects induced by the hard B2 BCC phase over the soft FCC one, as it will be shown later. Here, Nano Measure 1.2 software was used to measure the lamella thickness at approximately 80 different positions to obtain the average lamella thickness provided above. It should be emphasized that these measurements were obtained at multiple distinct orientations to get an overall understanding of the lamellae thickness variation upon tensile testing.

Fig. 3 details a superimposition of the synchrotron diffraction patterns obtained by full integration along the azimuthal angle for different stress/strain levels during tensile testing. The phase identification detailed in Fig. 3 depicts that the as-cast $AlCoCrFeNi_{2.1}$ high entropy alloy is composed of a B2 BCC phase, a disordered FCC structure, an ordered FCC phase with $L1_2$ structure, and also a tetragonal phase, named as σ phase. The existing phases in the as-cast alloy are in excellent agreement with previous microstructural characterization performed using transmission electron microscopy on a similar alloy reported by Choudhuri et al. [53].

Of novelty within this work are the volume fraction quantification of the existing phases and the determination of their lattice parameters. These results are detailed in Table 2. The volume fraction of the FCC phase is 65.5% and within it exists the $L1_2$ FCC phase with a volume fraction of 0.7%. As for the B2 BCC phase, a volume fraction of 32.7% was determined and the σ phase, which is known to precipitate in the B2 BCC matrix upon solidification of the alloy [53], has a volume fraction of 1.1%. The measured lattice parameters for the two major phases that compose this eutectic alloy (disordered FCC and B2 BCC) are in good agreement with the work of Xiong et al. [87].

Confirmation of the presence of the $L1_2$ FCC phase is aided by the presence of a superlattice reflection of the (1 0 0) plane [88] (refer to Fig. 3). Previously, σ phase was identified (but not quantified) in $AlCoCrFeNi_{2.1}$ high entropy alloys [53,89,90], and this phase was also observed in an $Al_{0.5}CoCrFeMnNi$ alloy [40]. The ability to detect and

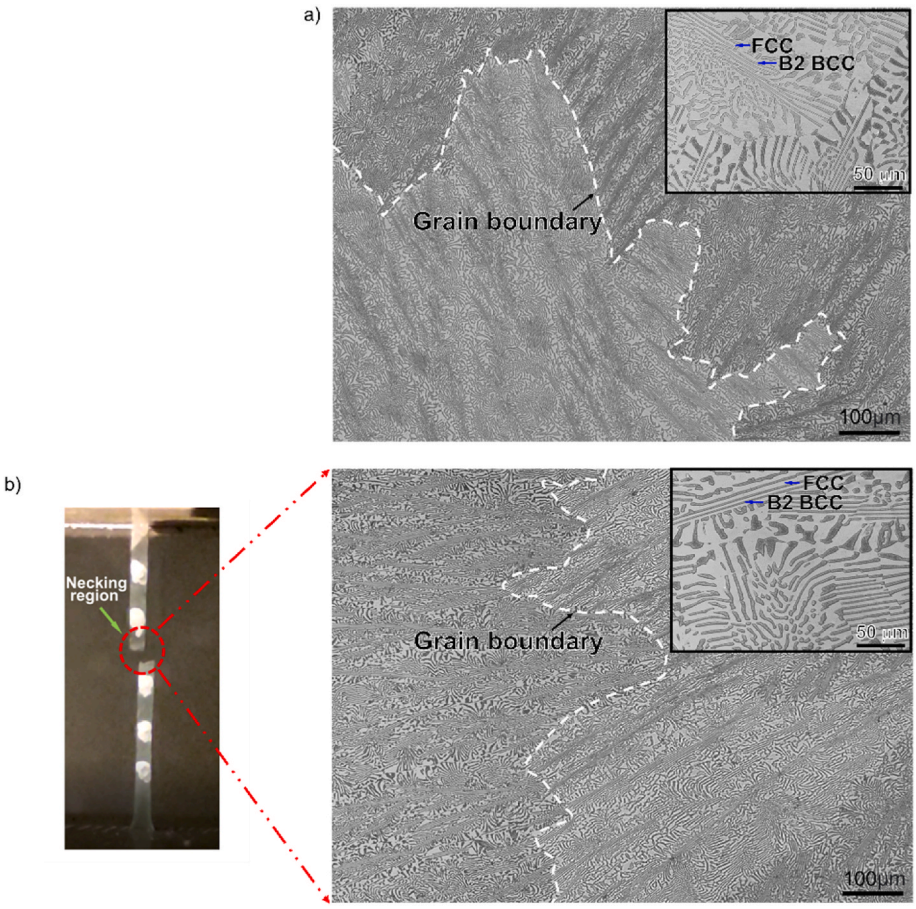

Fig. 2. Optical microscope images of as-cast $AlCoCrFeNi_{2.1}$ eutectic high entropy alloy: a) before tensile loading; b) after fracture. The inserts detail a close-up view of the lamellar structure.

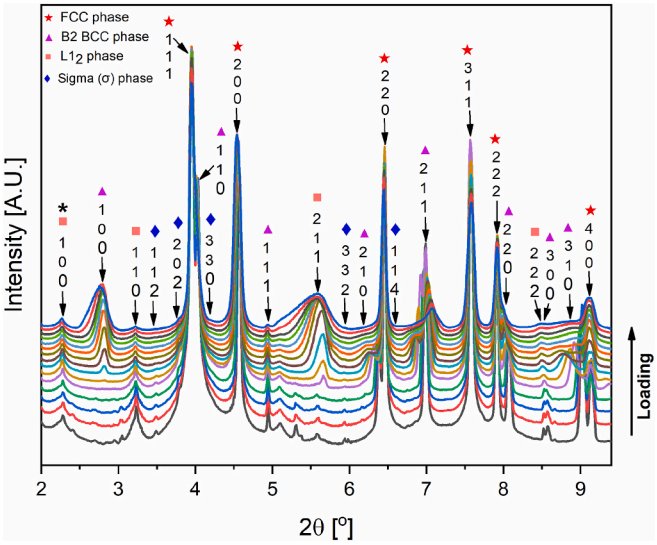

Fig. 3. Superimposition of the diffraction patterns obtained after integration of the Debye-Scherrer rings along the full azimuthal angle. * Marks the superlattice reflection of (1 0 0) $L1_2$ FCC phase.

quantify, for the first time, such low fraction phases ($L1_2$ FCC and σ phases) is related to the high signal-to-noise ratio enabled by high energy synchrotron X-ray diffraction. It should be noted the lattice parameters of the σ phase present in the eutectic alloy are similar to those reported for a related phase that can form in equiatomic CoCrFeMnNi high entropy alloy [91].

To further understand the initial as-cast material texture, the pole figures of the FCC and B2 BCC phases are given in Fig. 4. From Fig. 4 a), it can be seen that for the FCC phase, it has a preferential orientation of [111]//Z, although the texture is weak. For the B2 BCC phase (refer to Fig. 4 b)), there are preferential orientations for [110]//Z and [111]//X, but the textures are also weak. Based on the numerical information of the texture intensity for both FCC and B2 BCC phases, it can be said that the initial as-cast material before tensile deformation has no strong texture, and this can be described as a near-random texture. Indeed, the studied material did not undergo a thermomechanical treatment (e.g., rolling or rolling + heat treatment) and did not present significant texture as the material used in this work was removed from the centre of the ingot where the solidification conditions do not induce such a strong microstructure orientation, as it occurs near the cast walls, for example. Since the analyzed material was not rotated during tensile loading, it is not possible to quantitatively infer on the texture variation during tensile deformation, which is also outside the scope of our current research work. Here, it should be mentioned that X, Y and Z directions correspond to the loading direction, transverse direction (perpendicular to the loading direction) as well as the beam path direction, respectively (refer to Fig. 1).

3.2. *Macroscopic mechanical behavior, stress partitioning, and dislocation density evolution*

Fig. 5 details the engineering and true stress-strain curves (black and red lines, respectively), as well as the strain-hardening rate response

Table 2
Refined lattice parameters and volume fraction of the existing phases in the as-cast $AlCoCrFeNi_{2.1}$ high entropy alloy.

Phases	a [Å]	b [Å]	c [Å]	α [°]	β [°]	γ [°]	Space group	Volume fraction [%]
FCC	3.56232	a = b = c	a = b = c	90	90	90	Fm–3m	65.5 ± 0.75
B2 BCC	2.85168	a = b = c	a = b = c	90	90	90	*Pm*–3m	32.7 ± 0.41
$L1_2$ FCC	3.56219	a = b = c	a = b = c	90	90	90	*Pm*–3m	0.70 ± 0.05
σ	8.1768	a = b	5.0185	90	90	90	$P4_2/mnm$	1.1 ± 0.27

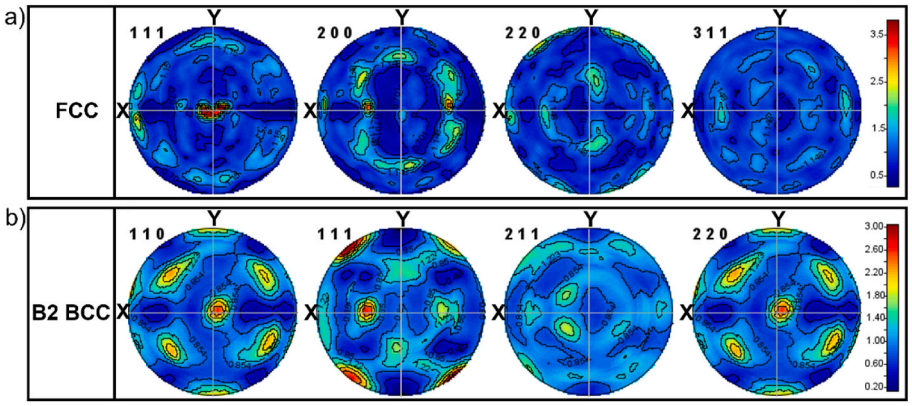

Fig. 4. Plot of pole figures of FCC and B2 BCC phase in as-cast $AlCoCrFeNi_{2.1}$ eutectic high entropy alloy in MAUD software using coverage of 5° cell size.

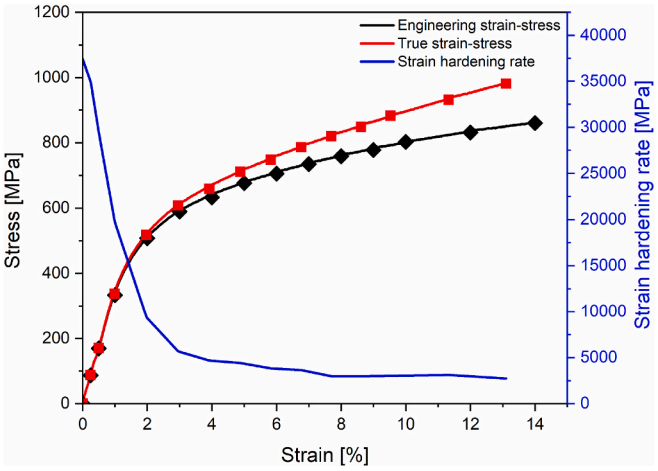

Fig. 5. Tensile strain-stress curves and strain hardening behavior of the as-cast $AlCoCrFeNi_{2.1}$ high entropy alloy.

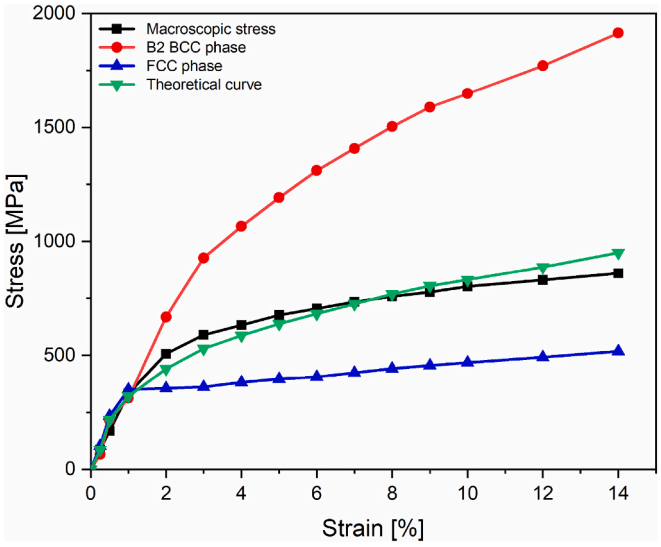

Fig. 6. Stress partitioning of B2 BCC phase and disordered FCC phase during in-situ synchrotron tensile loading.

(blue line) of the eutectic alloy. These results highlight that the $AlCoCrFeNi_{2.1}$ high entropy alloy in the as-cast condition has a combination of high strength and ductility. A tensile strength of 980 MPa and an elongation to fracture of 13.1% (true values) were measured. Macroscopically, the as-cast $AlCoCrFeNi_{2.1}$ high entropy alloy also exhibits extraordinary work-hardening behavior by comparison with NiAl-based alloys [92] and with other conventional engineering alloys [93]. Here, it should be mentioned that the strain-hardening curve is obtained from true stress-strain data.

To clarify the contributions of the two major phases in the alloy towards the work hardening behavior, the stress partitioning between the disordered FCC and ordered B2 BCC phases during macroscopic loading was determined, as previously detailed in the experimental section. These results are depicted in Fig. 6 and were obtained from the full azimuthal integrated data to evaluate the macroscopic mechanical response of both phases. From this data, it is evident that the macroscopic yield point of the material (≈333 MPa and 1.5% strain) corresponds to an abrupt point after which there is a significant stress redistribution between the FCC and B2 BCC phases. Comparing the individual stress-strain responses of the FCC and B2 BCC phases, it is perceptible that, within the elastic deformation regime, the FCC phase has a lower Young's modulus than the B2 BCC phase. The difference in elastic modulus between the hard B2 BCC and soft FCC phases ($E_{B2\ BCC} > E_{FCC}$) makes the FCC phase subjected to experience higher deformations for the same externally applied stress during macroscopic elastic deformation. Upon the initial yielding of the material, the stress partitioned to the B2 BCC phase (red line in Fig. 6) presents a steep and continuous rise, while the stress imparted by the FCC phase only increases by ≈ 150 MPa up until fracture, while for the B2 BCC phase the stress difference between the onset of yielding and fracture is of nearly ≈ 1600 MPa. Here, it should be mentioned that the lower yield strength of the FCC phase compared to the B2 BCC phase is derived from Fig. 6, blue and red lines, respectively. Specifically, comparing the yield points

of these two curves, it can clearly be observed that the FCC phase (blue line) yields at around 320 MPa, while the B2 BCC phase (red line) yields at about 800 MPa. Also, the yield point corresponds roughly to the abrupt point in the curve. However, the fundamental cause for this phenomenon is related to the behavior of the stress partitioning between the soft FCC and hard B2 BCC phases during tensile deformation and the resulting counteraction (i.e., reaction force) of the different dislocation densities evolutions on the strength increase between the two phases. Furthermore, the soft FCC phase is subjected to more load at the beginning of material deformation, while the B2 BCC phase imparts less load due to its harder nature. With further increase of the load, the soft FCC phase starts to yield, while the hard B2 BCC phase is still in the elastic deformation stage due to the non-existence of an effective load transfer mechanism from FCC to the B2 BCC phase. Plastic deformation is delayed until the soft FCC phase yields and the external load begins to be transferred to the hard B2 BCC phase.

We now consider the dislocation density evolution effect due to the different mechanical response of the two phases, and its strengthening effect. Theoretically, the dislocation density is proportional to dislocation strengthening, i.e., a high dislocation density induces a high strengthening effect. However, interestingly, for the cast $AlCoCrFeNi_{2.1}$ eutectic high entropy alloy studied in this work, it can be seen that the dislocation density in the B2 BCC phase induced a significantly higher strengthening effect than the FCC phase, although the FCC phase always had a higher dislocation density throughout the whole tensile process (refer to Fig. 8). This is related to the different strengthening contribution from dislocations between each phase where, as detailed in the experimental procedure, it was shown that the same increase in dislocation density for both phases will result in a higher strengthening effect induced by the B2 BCC phase.

Besides, the lower stress difference between yield and fracture of the FCC phase (about 150 MPa) is mainly related to the different mechanical responses exhibited by the FCC and B2 BCC phases during the tensile loading process. In other words, this is related to the stress partitioning between the FCC and B2 BCC phases during tensile loading and to the strain-hardening behaviour of the two phases which possess different mechanical response under loading. As mentioned above, during the elastic deformation stage, due to the soft nature of the FCC phase compounded by the hard response of B2 BCC phase, the FCC phase bears more stress first. Upon further loading up to about 320 MPa, the FCC phase starts to yield (as shown by the blue line in Fig. 6), however, the B2 BCC phase is still in the elastic domain, which is due to the majority of the stress being imparted by the soft phase. Eventually, as the externally imposed loading continues to increase, more load starts to be transferred to the hard B2 BCC phase. In addition, in this stage, the plastic deformation of the soft FCC phase is also constrained by the surrounding hard B2 BCC phase, in which this phase acts as a physical barrier to the deformation of the FCC phase. Following this, once the hard B2 BCC phase also yields, due to differences in the mechanical response of both phases, both FCC and B2 BCC exhibit different hardening behaviours, where the hard B2 BCC phase exhibits a significantly higher strain-hardening behavior. Different from the high-strain hardening behaviour exhibited by the hard B2 BCC phase, the soft FCC phase presents an almost negligible work-hardening behavior after the onset of plastic deformation.

Further analysis of Fig. 6 suggests that yielding of the hard B2 BCC phase only starts to occur for a macroscopic strain of 3.5%, after which a non-linear elastic response is observed. This behavior is also observed in the lattice strain evolution (refer to Fig. 11 and subsequent discussion). Furthermore, a distinctive behavior between both phases is evident: the softer FCC phase has an almost negligible work hardening behavior since after the onset for plastic deformation its phase stress remains almost unchanged. The same does not occur for the B2 BCC phase, where significant work hardening exists right after the end of the elastic deformation region. Therefore, it can be concluded that the macroscopic work hardening behavior of the as-cast $AlCoCrFeNi_{2.1}$ eutectic high entropy alloy is predominantly arising from the B2 BCC phase. It should be noticed that these phase stress calculations were made considering the (3 1 1) FCC and (2 1 1) B2 BCC planes, as these are less affected by intergranular stresses and can provide a more precise understanding of the load partitioning experienced by the material. Although significant differences between the FCC and B2 BCC phases are observed during plastic deformation, the same does not occur during macroscopic elastic loading where there is no evident load partitioning.

Another interesting point arising from the phase partitioning data concerns the possibility to tune the mechanical response of eutectic high entropy alloys based on the volume fraction of both FCC and BCC phases. From this data, it can be seen that higher strength levels can be achieved by a material with a higher volume fraction of the B2 BCC phase, whereas if lower strength but increased ductility is required then the volume fraction of the FCC phase must increase. The load partition and the higher stresses that are transferred to the B2 BCC phase also highlight that this is the strengthening phase for the present eutectic high entropy alloy. When considering the stress transferred to each phase and the respective volume fraction, the resulting curve (green line in Fig. 6) is in good agreement with the macroscopic tensile behavior of the alloy (black line in Fig. 6).

To showcase the strengthening effect of the B2 BCC phase as a function of different volume fraction contents, Fig. 7 was developed to further highlight the relative importance of each phase for the overall material strength. It should be emphasized that these calculations can only be used to evaluate the potential strength of the alloy and not its ductility.

The dynamic evolution of the dislocation density in both disordered FCC and ordered B2 BCC phases is qualitatively analyzed next. Fig. 8 (a, c, and e) depicts the average lattice strain, ε_0, as a function of engineering strain for both FCC and B2 BCC phases along LD, TD, and for full azimuthal integration, respectively, while Fig. 8 (b, d, and f) illustrates the dislocation density evolution for the same conditions. Fig. 9 details the strengthening effect promoted by the dislocation density evolution in both FCC and B2 BCC phases.

The evolution of the average lattice strain, ε_0, for both phases depicts that the FCC phase has a slightly higher ductility than the B2 BCC phase regardless of whether to consider the LD (Fig. 8 a) or TD (Fig. 8 c), or even the overall material behaviour (Fig. 8 e). These results, in combination with the stress partitioning data (Fig. 6), further emphasize that the material strength is primarily controlled by the volume fraction of the B2 BCC phase, while its ductility can be regulated by the disordered

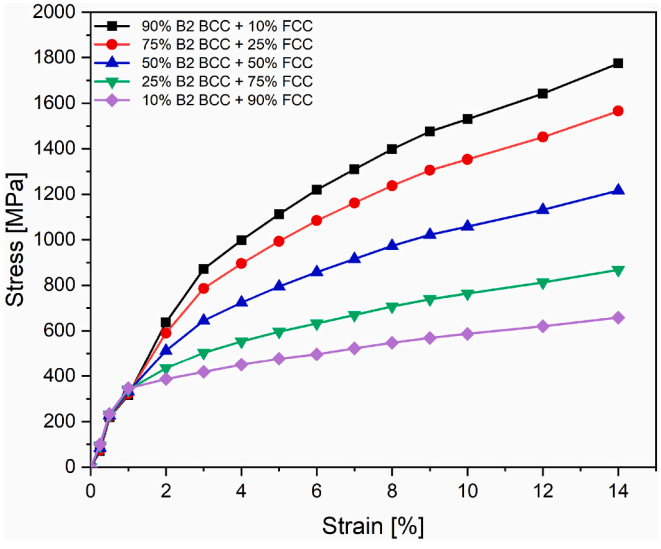

Fig. 7. Calculated effect of different volume fractions of disordered FCC and ordered B2 BCC on the mechanical response of the eutectic high entropy alloy.

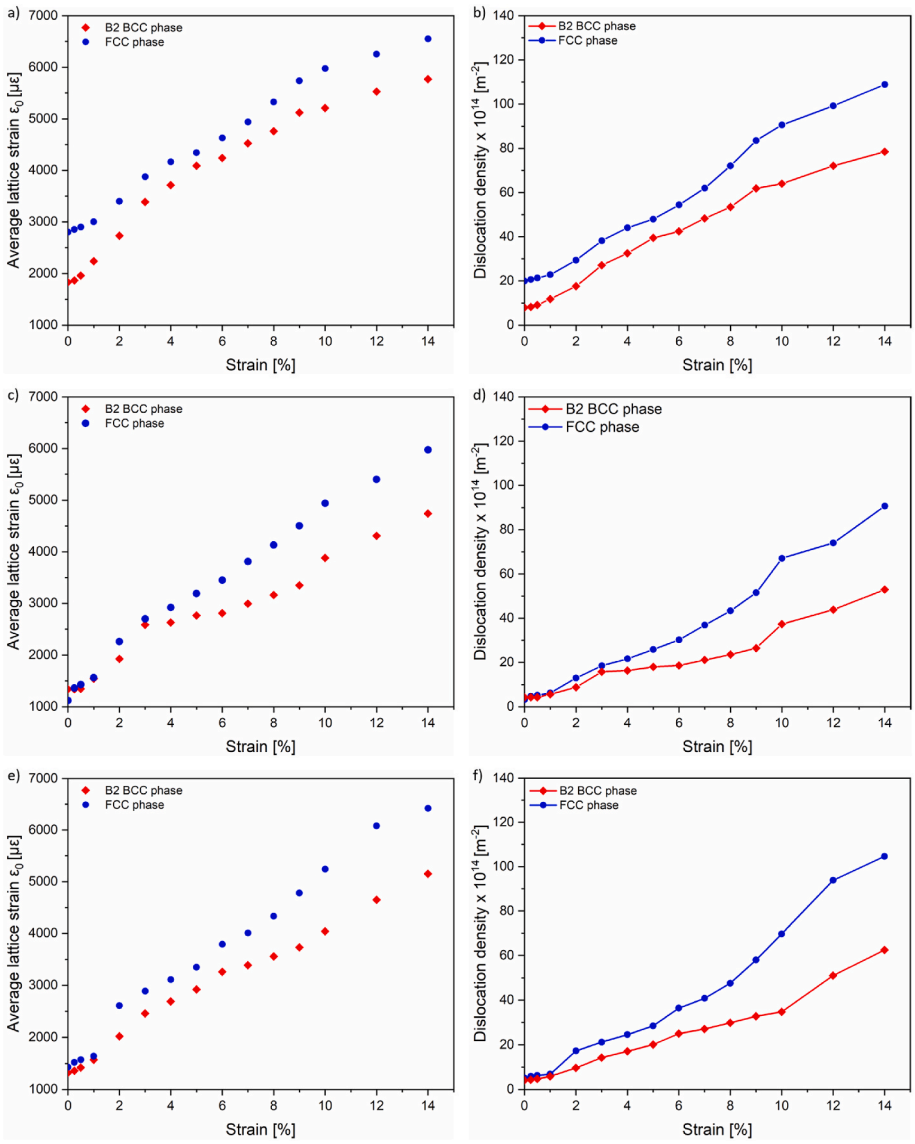

Fig. 8. a), c) and e) Evolution of the average lattice strain, ε_0, as a function of engineering strain along LD, TD and full azimuthal angle integration; b), d) and f) dislocation density evolution as a function of engineering strain along LD, TD and full azimuthal integration, respectively. For the same analyzed microstructure feature (average lattice strain or dislocation density) the y axis range is kept the same to properly evaluate orientation-dependent changes.

FCC phase. Also, regardless of the orientation considered, the dislocation density in the FCC phase is always higher than that in the B2 BCC phase. Moreover, the dislocation density determined along the LD (Fig. 8 b) is higher than that determined along TD (Fig. 8 d), which is expected since preferential (plastic) deformation will primarily occur along the loading axis. The bulk dislocation density of both phases (Fig. 8 f) considers all variations of the dislocation density across the full azimuthal range and lies between the measured maximum (along LD) and the minimum (along TD) values. Further discussion is detailed next considering the full azimuthal integrated data, since there are no major differences for this alloy system when considering a specific principal orientation (LD or TD) vs full azimuthal integration.

In the as-received condition, i.e., prior to any mechanical loading, the dislocation density was similar for both phases, 5.2×10^{14} and 4.1×10^{14} m^{-2} for the FCC and B2 BCC phases (refer to Fig. 8 f), respectively. These dislocation density values are within the order of magnitude for other high entropy alloys, such as CoCrFeNi and CoCrFeMnNi, in their as-cast state and as-rolled state [94,95].

During the elastic deformation domain, the dislocation densities of both the FCC and B2 BCC phases do not change significantly, but the dislocation density of the B2 BCC phase is always slightly below that of the FCC phase. This evolution is consistent with a similar variation trend exhibited in the phase stress partitioning in the elastic region ($\varepsilon < 1.5\%$), as previously shown in Fig. 6.

When the applied strain increases above 1.5%, the material starts to deform plastically. The dislocation density of the FCC phase increases significantly to 1.9×10^{15} m^{-2}, while the B2 BCC phase only shows a moderate increase to 9×10^{14} m^{-2}. The reason for the difference in the evolution of dislocation density between these two phases is that under externally applied stresses, the plastic deformation of the eutectic alloy is activated in the FCC phase first due to the inherent soft nature of this phase (nanohardness of the FCC and B2 BCC phases of 5.8 ± 0.2 GPa and B2 BCC $= 9.7 \pm 0.3$ GPa, respectively [34]). Therefore, when plastic deformation in the FCC phase is induced there is a concomitant increase in the number of dislocations that are formed, thus justifying the increased dislocation density over that of the BCC phase.

During the macroscopic plastic deformation regime, the dislocation density evolution in both phases tends to increase almost linearly up until fracture. However, the increased slope of the curve corresponding to the FCC phase highlights that the strengthening mechanism induced

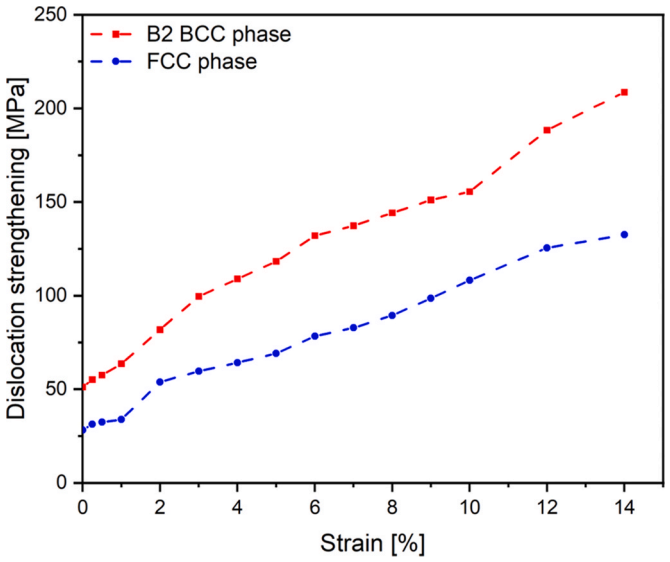

Fig. 9. Evolution of the dislocation strengthening for the FCC and B2 BCC phases considering full azimuthal data.

by the generation and movement of dislocations is not as effective in promoting the strain hardening of the alloy. This is further elucidated in the evolution of the alloy strengthing induced by the variation of the dislocation density in both phases, as detailed in Fig. 9. In fact, it is observed that the increase in alloy strength due to the dislocation density in the B2 BCC phase is significantly higher (≈100 MPa) than that caused by the increase in dislocation density in the FCC phase, even though this latter phase has always a higher dislocation density throughout the tensile test.

Due to the stress incompatibility between the FCC and B2 BCC phases which arises from their distinct mechanical behaviour (as shown in Fig. 6), the soft FCC matrix plastically deforms first, leading to the proliferation and rearrangement of dislocation substructures, resulting in a substantial increase in dislocation density [26]. Plastic deformation of the hard B2 BCC phase is delayed until effective stress transfer to this phase occurs. At this time, the plastic deformation experienced by the B2 BCC phase results in increased dislocation density, as previously shown in Fig. 8 (c). In reality, plastic deformation of the soft FCC phase is constrained by the hard B2 BCC. The FCC phase cannot plastically deform in a free way, because of the lamellar structure of the eutectic phase: the hard B2 BCC acts as a physical barrier to the deformation of the FCC phase. This leads to the formation of strain gradients across the FCC + B2 BCC eutectic structure [26]. It should be emphasized that such strain gradients will increase with proceeding deformation because of the distinct mechanical behaviours of the FCC and B2 BCC phases. In fact, the different mechanical properties of the FCC and B2 BCC phases are known to generate a back-stress that can also increase the strength of the alloy [26]. The mechanism that promotes this back-stress is described next. The deformation of the soft FCC is constrained by the hard B2 BCC phase, which aids in the formation of strain gradients across both phases. More dislocations are formed in the FCC phase since this phase will always bear more plastic strain than the B2 BCC one. This continues to increase the strain gradient across the eutectic microstructure. Directly resulting from these strain gradients, there is an increase in the geometrical necessary dislocations (GND) which then promotes a strength increase by the resulting back-stresses. Since the FCC phase is significantly more deformed and is also constrained by the B2 BCC phase during deformation it will necessarily generate more dislocations when macroscopic deformation is progressing, thus justifying the higher dislocation density across the tensile test. Such back-stress effects have been exemplified in the literature when developing similar eutectic high entropy alloys possessing hierarchical microstructures [26]. There is a final potential contributing factor to the alloy strength which is related to an ordering strengthening mechanism induced by the B2 phase.

To further verify the dynamic microstructure evolution and fracture mechanism, Fig. 10 b1-b4) presents kernel average misorientation (KAM) maps obtained at different distances from the fracture site. The A0 region is the furthest from the fracture site and corresponds to the non-deformed region. For A1, A2, and A3, the distance from the fracture site gradually decreases, which corresponds to an increase in the experienced deformation.

A KAM map is defined as the misorientation around a measured point with respect to a defined set of nearest neighbours' points and can be used to infer the dislocation density, as well as the amount of strain imparted by the different phases that exist in the material. From Fig. 10 b1) to b4), it can be noticed that the average KAM value increases in the following order: $A0_{KAM\approx1.1^\circ} < A1_{KAM\approx1.35^\circ} < A2_{KAM\approx2.21^\circ} < A3_{KAM\approx2.24^\circ}$, and the closer to the fracture site, the greater the increase of the average KAM value. This indicates that the A3 region, closest to the fracture site, accommodates the largest plastic deformation during tensile deformation, followed by A2 and A1, and finally the smallest deformation occurs in the A0 region. The specific evolutions of the average KAM values for the four measured regions are detailed in Fig. 10 c1). Considering that the $AlCoCrFeNi_{2.1}$ eutectic high entropy alloy does not suffer from phase transformation during the tensile loading process, the effect of any phase transformation on the fracture mechanism can be excluded. It can be assumed that near the fracture site (A3 region), the stress concentration first appears due to the existence of the previously identified nanoprecipitated phases (Refer to Fig. 3), which in turn leads to this region preferentially bearing more stress and plastic deformation under the tensile loading, eventually leading to fracture.

As a further insight into the evolution of the dislocation density in the two matrix Phases (FCC and B2 BCC) during tensile deformation, the KAM values of the two matrix phases in these regions (A0, A1, A2, and A3) are provided in Fig. 10 c3). Specifically, the solid and dashed lines represent the variations of the KAM values in the FCC and B2 BCC matrix phases, respectively, with the different colors corresponding to different regions. Not surprisingly, the average KAM values in both the FCC and B2 BCC phases increase with decreased distance from the fracture site, which qualitatively revealed that the dislocation density in both matrix phases increases with increasing deformation. This tendency is consistent with the results calculated using synchrotron diffraction techniques (refer to Fig. 8 f)). Besides, comparing the average KAM value in the FCC (solid line) and B2 BCC phase (dashed line) within the same region (refer to the inserted table in Fig. 10 c2), it can be seen that the average KAM value with the FCC phase is higher than that in the BCC phase over all regions (A0 - A3), which implies that the dislocation density in the soft FCC phase under the same load during tensile deformation is higher than in the hard B2 BCC phase, this owing to the different mechanical response during loading of the dual phase FCC + BCC structure the KAM evolution is certainly distinct, which, again, matches well with the results calculated by synchrotron X-ray diffraction data (Fig. 8 f)).

3.3. Lattice strain evolution

Fig. 11 depicts the evolution of the lattice strains for the (2 0 0), (3 1 1), (2 2 2) planes of FCC, (2 1 1), (1 1 0), (3 1 0) planes of B2 BCC, and (1 0 0) plane of $L1_2$ FCC parallel (LD) and perpendicular (TD) to the loading direction. When the engineering stress is less than 333 MPa (corresponding to 1.5% strain) the lattice strain of all planes has a linear response with the applied stress (refer to Fig. 11 (a1), (b1), and (c1)). This shows that up to this point the material is only being elastically deformed, thus in good agreement with the stress partitioning and tensile response of the eutectic alloy.

Linear fitting of the evolution of the lattice strain with the macroscopic stress for each lattice plane allows for determining the direction-dependent Young's modulus. Lattice strain evolution along the loading

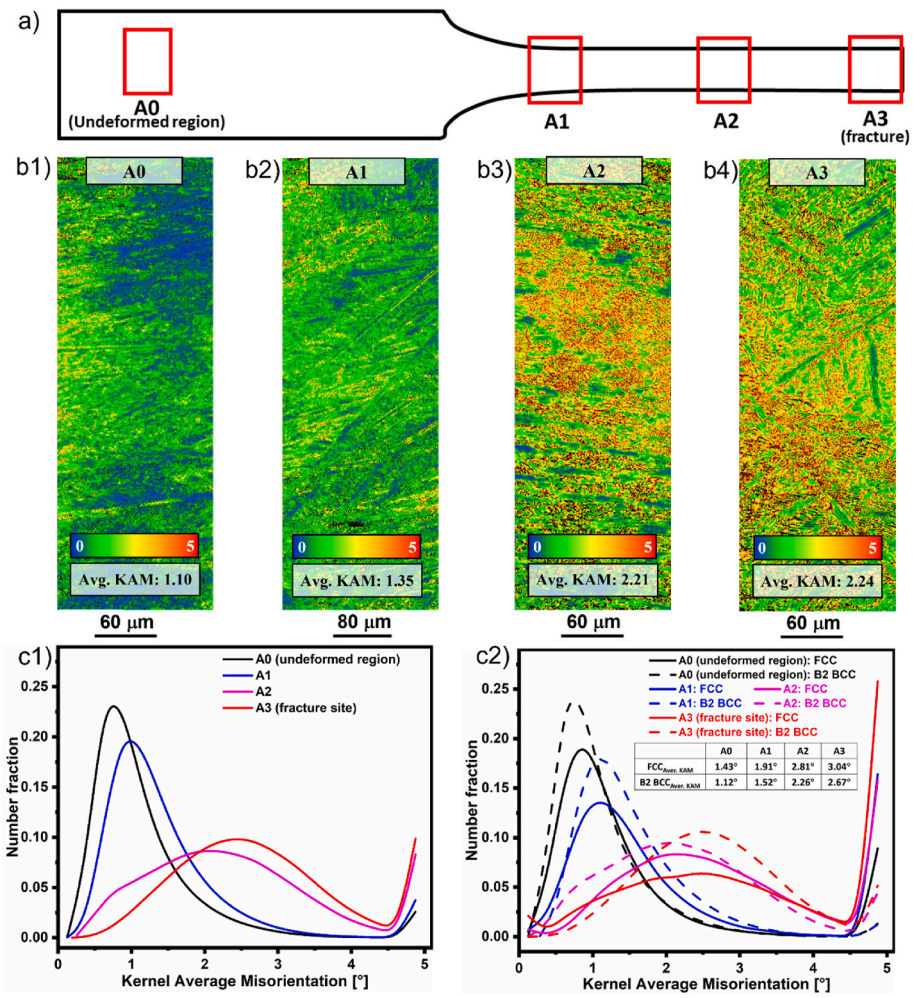

Fig. 10. a): Schematic of the tensile specimen after fracture; b1-b4): EBSD KAM maps at different distances from the fracture location, corresponding to the red box A0 (undeformed region), A1, A2, and A3 (fracture site), respectively, as marked in Fig. 9 a); c1): variation of KAM values among A0, A1, A2 and A3 regions; c2): variation of KAM values with respect to the different phase structures in regions of A0, A1, A2, and A3. (For interpretation of the references to color in this figure legend, the reader is referred to the Web version of this article.)

direction (LD) and transverse direction (TD) as a function of applied stress (a1, b1, c1), strain (a2, b2, c2) and partitioned stress (a3, b3, c3) for FCC (a1, a2, a3), B2 BCC (b1, b2, b3) and $L1_2$ FCC phases (c1, c2, c3) reveals different behaviors for both phases and crystallographic planes. The dashed lines represent the onset for macroscopic plastic deformation. The inserts in Fig. 11 b1), b2) and b3) detail close up of the lattice strain variation for the selected lattice planes.

Table 3 details the Young's modulus for all analyzed planes obtained in the LD, revealing strong elastic anisotropy. For the FCC phase, the (2 2 2) plane has the largest elastic modulus (265 GPa), whereas the (2 0 0) plane has the lowest with 108 GPa. This means that the (2 0 0) plane is the softest, while the (2 2 2) is the hardest. These results are in good agreement with previous work by Lu et al. on the $AlCoCrFeNi_{2.1}$ eutectic high entropy alloy [54]. As for the B2 BCC phase, the hardest plane was the (2 1 1), while the (3 1 0) is the softest (191 vs 108 GPa).

Another novelty of this work is the determination of the superlattice (1 0 0) plane elastic modulus for the $L1_2$ FCC phase which was calculated to be 222 GPa. Calculations for other planes were not performed owing to the extremely low intensity of the diffraction peaks and overlapping, which prevented an accurate implementation of the peak fitting procedure described in the experiment and methods section.

Attention is now paid to the lattice strain evolution when macroscopic plastic deformation starts to occur. When the material enters the plastic deformation stage, a nonlinear response for all lattice planes with increased applied stress gradually becomes more evident. The deviation from linearity, which corresponds to the onset for macroscopic plastic deformation, has been marked with a dashed horizontal line in Fig. 11 a1), b1), and c1) for the FCC, B2 BCC, and $L1_2$ FCC phases. It has been demonstrated that the separation of lattice strains in different phases or different grain families in the plastic region, indicates the occurrence of stress redistribution between different phases and grain families [96–98]. This is again in excellent agreement with the phase stress partitioning calculations previously shown in Fig. 6. In this case, the internal stress is transferred from the soft phase or the soft grain family to their hard counterparts after plastic deformation in the soft domain. Here, it is worth noting that the root cause of the stress redistribution that occurs among the different grain families described above does not come from the 14% macroscopic strain itself but is associated to the partitioned stress of the phases (FCC and B2 BCC) in which the grain families are located during tensile deformation. A more detailed explanation will be provided in the section focusing on the relationship between the phase partitioned stress and lattice strain evolution.

Comparing the lattice strain distributions of the FCC and B2 BCC phases along the LD (refer to Fig. 11 a2) and b2)), it can be observed that the lattice strains of all analyzed planes of the FCC phase start to deviate from a linear elastic response after the macroscopic yield point (333 MPa), which indicates that the FCC phase yields first than the B2 BCC phase as previously shown and discussed considering the macroscopic response of the alloy detailed in Fig. 6. Also, the lattice strain of all analyzed planes of the B2 BCC phase is significantly larger than those of the FCC planes. For example, the maximum lattice strain of the (h k l) planes of the B2 BCC phase corresponded to the (3 1 0) lattice plane which is almost 8 times higher than the largest lattice (h k l) strain of the FCC phase, which corresponded to the (2 0 0) plane. Quantitatively, this translates to a maximum lattice strain of ≈65000 με for the (3 1 0) B2 BCC plane and ≈8000 με for the (2 0 0) FCC plane. As for the TD, larger

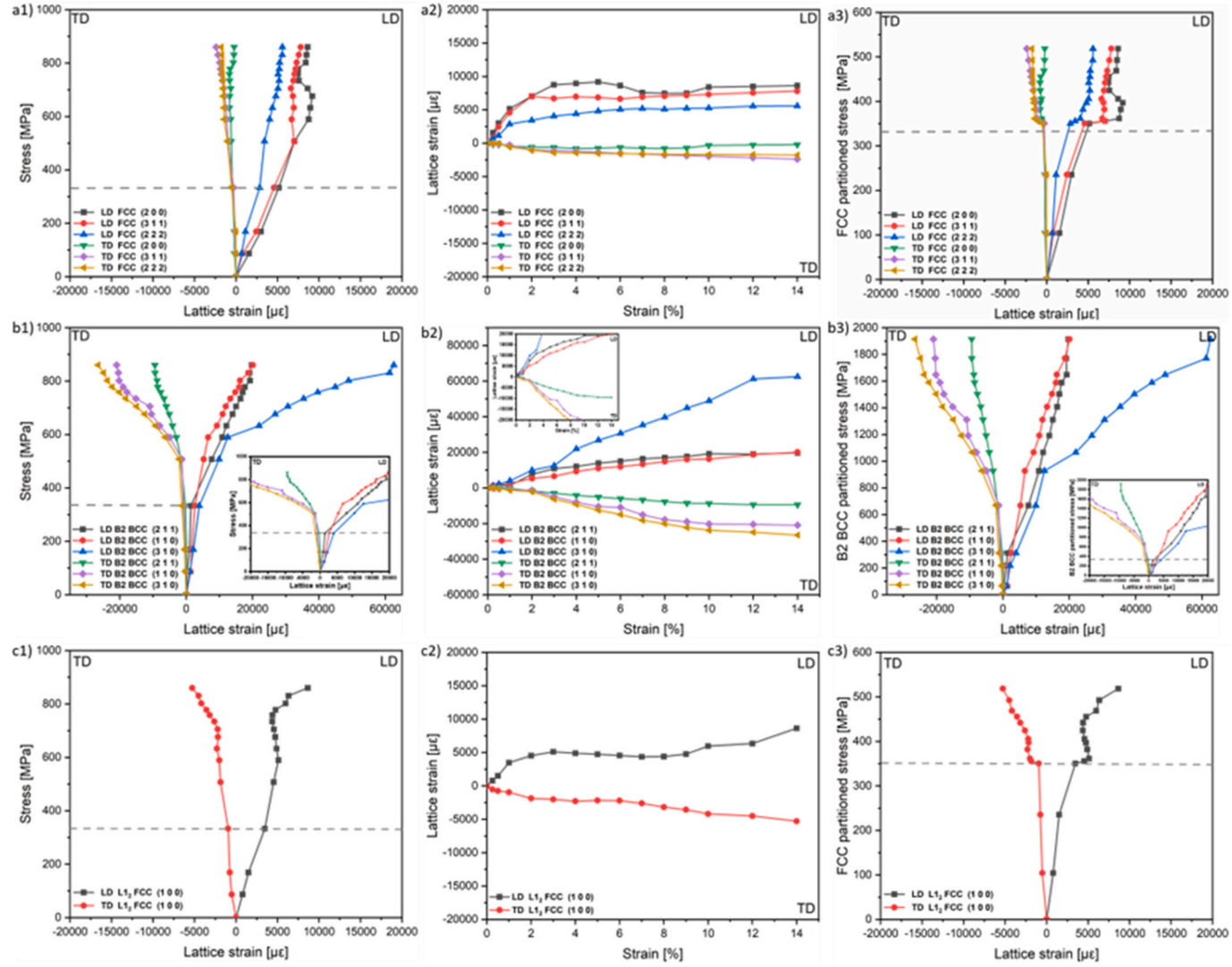

Fig. 11. Lattice strain evolution along the loading direction (LD) and transverse direction (TD) as a function of applied stress (a1, b1, c1), strain (a2, b2, c2) and partitioned stress (a3, b3, c3) for FCC (a1, a2, a3), B2 BCC (b1, b2, b3) and $L1_2$ FCC phases (c1, c2, c3). The dashed lines represent the onset for macroscopic plastic deformation. The inserts in Fig. 11 b1), b2) and b3) detail close up of the lattice strain variation for the selected lattice planes.

Table 3
Elastic modulus for different lattice planes of constituent phases in as-cast $AlCoCrFeNi_{2.1}$ high entropy alloy.

$L1_2$ FCC phase	FCC phase			B2 BCC phase		
E_{100} (GPa)	E_{200} (GPa)	E_{311} (GPa)	E_{222} (GPa)	E_{211} (GPa)	E_{110} (GPa)	E_{310} (GPa)
222	108	221	265	191	175	108

lattice strains are preferentially obtained in the analyzed B2 BCC planes. This behavior could indicate that preferential macroscopic deformation should be expected in the B2 BCC phase, which was not experimentally observed as previously shown. The reason that justifies the increased lattice strains for the analyzed B2 BCC planes is related to the preferential deformation in the two analyzed directions, i.e., parallel and perpendicular to the loading direction. In fact, this preferential deformation, which is governed by the material texture, depends on the spatial relationship between a certain (h k l) plane and the azimuthal angle. Although not shown here, when analyzing other azimuthal angle ranges ($30° \pm 7.5°$, $45° \pm 7.5°$, and $60° \pm 7.5°$) larger lattice strain deformations in the FCC planes were observed, thus further confirming the dependence of the lattice deformation with the azimuthal angle.

A closer look at the superlattice reflection of the (1 0 0) plane of the $L1_2$ FCC phase (refer to Fig. 11 c1) reveals near mirror-like behavior, with a maximum positive lattice strain of ≈8000 με developing along the LD and maximum negative lattice strain of ≈5000 με developing in the TD. Further observation of the lattice strain evolution of the (1 0 0) $L1_2$ FCC superlattice plane and the (2 0 0) FCC lattice plane under tensile loading, revealed that the two planes have similar deformation evolution (as shown in Fig. 11 a1) and c1)). The $L1_2$ FCC phase coherently precipitates within the FCC matrix, thus it is expected that equivalent crystallographic planes behave similarly. This is what is observed when directly comparing the (1 0 0) $L1_2$ FCC superlattice plane to the (2 0 0) plane of the surrounding matrix. The interaction mechanism of secondary phases with dislocations usually includes dislocation cutting and Orowan looping mechanisms [99]. The interaction mechanism of the $L1_2$ phase as the secondary phase with dislocations during deformation is considered as dislocation cutting [39]. The dislocation-cutting mechanism is mainly manifested by the dislocation cutting through the second phase and deforming it along with the matrix phase. This explains why the $L1_2$ FCC phase has a similar deformation behavior to that of the FCC matrix phase (Fig. 8 e) and f).

To further visualize the relationship between the lattice strain and

the partitioned stress for the existing phases, Fig. 11 a3), b3) and c3) detail these variations along the TD and LD directions. First of all, as can be seen in Fig. 11 a3), the mechanical response of different lattice planes in the FCC is similar to the phase stress partitioning behavior in FCC phase (refer to the blue curve of Fig. 6), both yielding at about 350 MPa. After yielding, the FCC phase starts to deform plastically. From the evolution of the partitioned stress and lattice strain for the different lattice planes of the FCC after phase yielding, there is almost no significant work-hardening effect. Similarly, the $L1_2$ FCC (1 0 0) lattice plane does not exhibit appreciable work-hardening. Considering now the B2 BCC phase, the yield point of each lattice plane is significantly higher than the macroscopic yield point of the material as well as the yield point of each lattice plane in the FCC phase ($\approx$ 900 MPa vs. $\approx$ 350 MPa). Also, after the B2 BCC phase yields, all lattice planes exhibit significant work-hardening behavior. In particular, the (3 1 0) oriented grains deviate significantly to a larger lattice strain. Overall, the yielding and hardening behavior exhibited by each lattice plane within the FCC and B2 BCC phases with respect to the relationship between the phase partitioned stresses and lattice strain evolution, match well with the phase stress partitioning behavior they exhibit during tensile loading process.

Furthermore, from the perspective of the relationship between phase partitioned stress and lattice strain evolution, when the material enters the plastic deformation stage (at $\approx$ 350 MPa), the nonlinear response of all lattice planes in the FCC phase becomes more distinct, which is related to the phase yielding. Interestingly, the B2 BCC phase does not show a significant nonlinear response behavior with increasing stress after this material enters macroscopically yields, which is mainly associated with the inherent mechanical properties of the B2 BCC phase, including the high work-hardening, as well as the partitioning behavior to the FCC phase in the early deformation stage, which delays its yielding. Accordingly, the corresponding nonlinear behavior of all lattice planes in the B2 BCC phase becomes apparent only when their partitioned stresses reach $\approx$900 MPa.

4. Conclusions

The micromechanical behavior of an as-cast $AlCoCrFeNi_{2.1}$ eutectic high entropy alloy during tensile deformation has been investigated by in-situ tensile testing at room temperature using high energy synchrotron X-ray diffraction. The phase constitution and respective volume fractions, phase stress partitioning, dislocation density evolution as well as the lattice strain evolution parallel and perpendicular to the loading direction were determined. The following major conclusions can be drawn:

Phase identification of the as-cast eutectic alloy revealed the presence of two FCC phases (one ordered and one disordered), an ordered BCC phase, and a tetragonal σ phase. These results contradict several works on the phase identification of the same eutectic alloy, which often misidentify the existing phases. The lattice parameters of all four phases were determined: i) FCC, a = b = c = 3.56232 Å; ii) B2 BCC, a = b = c = 2.85168 Å; iii) $L1_2$ FCC, a = b = c = 3.56219 Å; iv) σ, a = b = 8.1768 Å, c = 5.0185 Å.

Stress partitioning between the two major matrix phases, FCC and B2 BCC, revealed that upon the onset of plastic deformation the stress is primarily transferred to the hard B2 BCC phase. Moreover, plastic deformation of the hard B2 BCC phase is delayed until a macroscopic strain of 3.5% is achieved. We also highlight the possibility to tune the stress/strain response of eutectic high entropy alloys by changing the volume fraction of the matrix phases. Change of the volume fraction of existing phase can be achieved by changes in the material composition and/or use of heat treatments.

The evolution of the dislocation density was seen to occur preferentially in the soft FCC phase. Nonetheless, the strength contribution resulting from the increase in dislocation density was calculated to be more significant in the B2 BCC phase, even though this phase has a smaller dislocation density than the FCC phase throughout the entire deformation.

The dynamic evolution of the continuously increasing dislocation density in the soft FCC and hard B2 BCC phases obtained from the synchrotron data is consistent with the evolution of KAM values obtained by EBSD. Furthermore, the increased dislocation density in the soft FCC phase coincides with the fact that the KAM values in the FCC phase are always higher than those in the B2 BCC phase throughout the whole tensile process.

The lattice strain evolution along the parallel and perpendicular directions to the loading in both cases revealed that the analyzed (h k l) planes of the B2 BCC phase present a significantly larger lattice strain than those of the FCC phase, this is mainly related to the different phase partitioned stress behavior.

CRediT authorship contribution statement

Jiajia Shen: Investigation, Formal analysis, Data curation, Methodology, Writing – original draft. **J.G. Lopes:** Investigation. **Zhi Zeng:** Investigation. **Yeon Taek Choi:** Investigation, Data curation, RG: Investigation, Formal analysis, Data Curation. **E. Maawad:** Investigation. **N. Schell:** Investigation. **Hyoung Seop Kim:** Investigation, Resources. **Rajiv S. Mishra:** Investigation, Resources, Writing – review & editing. **J.P. Oliveira:** Formal analysis, Resources, Validation, Conceptualization, Methodology, Writing – review & editing.

Declaration of competing interest

The authors declare that they have no known competing financial interests or personal relationships that could have appeared to influence the work reported in this paper.

Data availability

Data will be made available on request.

Acknowledgements

JS, JGL, and JPO acknowledge Fundação para a Ciência e a Tecnologia (FCT - MCTES) for its financial support via the project UID/00667/2020 (UNIDEMI). JS acknowledges the China Scholarship Council for funding the Ph.D. grant (CSC NO. 201808320394). JGL acknowledges FCT – MCTES for funding the Ph.D. grant 2020.07350.BD. JPO acknowledges funding by national funds from FCT - Fundação para a Ciência e a Tecnologia, I.P., in the scope of the projects LA/P/0037/2020, UIDP/50025/2020 and UIDB/50025/2020 of the Associate Laboratory Institute of Nanostructures, Nanomodelling and Nanofabrication – i3N. The authors acknowledge DESY (Hamburg, Germany), a member of the Helmholtz Association HGF, for the provision of experimental facilities. Beamtime was allocated for proposal I-20210899 EC. The research leading to this result has been supported by the project CALIPSOplus under the Grant Agreement 730872from the EU Framework Programme for Research and Innovation HORIZON 2020. HSK acknowledges the National Research Foundation of Korea (NRF) grant funded by the Korea government (MSIP) (NRF-2021R1A2C3006662, NRF-2022R1A5A1030054). Yeon Taek Choi was supported by the Basic Science Research Program “Fostering the Next Generation of Researcher” through the NRF funded by the Ministry of Education [grant number 2022R1A6A3A13073824].

The raw/processed data required to reproduce the above findings cannot be shared at this time as the data also forms part of an ongoing study.

References

[1] O.N. Senkov, G.B. Wilks, J.M. Scott, D.B. Miracle, Intermetallics Mechanical properties of Nb 25 Mo 25 Ta 25 W 25 and V 20 Nb 20 Mo 20 Ta 20 W 20

refractory high entropy alloys, Intermetallics 19 (2011) 698–706, https://doi.org/10.1016/j.intermet.2011.01.004.
[2] M. Zhang, X. Zhou, X. Yu, J. Li, Surface & Coatings Technology Synthesis and characterization of refractory TiZrNbWMo high-entropy alloy coating by laser cladding, Surf. Coating. Technol. 311 (2017) 321–329, https://doi.org/10.1016/j.surfcoat.2017.01.012.
[3] C. Lee, Y. Chou, G. Kim, M.C. Gao, K. An, J. Brechtl, C. Zhang, W. Chen, J. D. Poplawsky, G. Song, Y. Ren, Y.C. Chou, P.K. Liaw, Lattice-distortion-enhanced yield strength in a refractory high-entropy alloy, Adv. Mater. 32 (2020), https://doi.org/10.1002/adma.202004029, 1–9.
[4] B. Gwalani, V. Soni, M. Lee, S. Mantri, Y. Ren, R. Banerjee, Optimizing the coupled effects of Hall-Petch and precipitation strengthening in a Al 0.3 CoCrFeNi high entropy alloy, Mater. Des. 121 (2017) 254–260, https://doi.org/10.1016/j.matdes.2017.02.072.
[5] Z. He, N. Jia, H. Yan, Y. Shen, M. Zhu, X. Guan, X. Zhao, S. Jin, G. Sha, Y. Zhu, C. T. Liu, Multi-heterostructure and mechanical properties of N-doped FeMnCoCr high entropy alloy, Int. J. Plast. 139 (2021), 102965, https://doi.org/10.1016/j.ijplas.2021.102965.
[6] J.-K. Kim, J.H. Kim, H. Park, J.-S. Kim, G. Yang, R. Kim, T. Song, D.-W. Suh, J. Kim, Temperature-dependent universal dislocation structures and transition of plasticity enhancing mechanisms of the Fe40Mn40Co10Cr10 high entropy alloy, Int. J. Plast. 148 (2022), 103148, https://doi.org/10.1016/j.ijplas.2021.103148.
[7] C. Shang, E. Axinte, J. Sun, X. Li, P. Li, J. Du, P. Qiao, Y. Wang, CoCrFeNi (W 1 − x Mo x) high-entropy alloy coatings with excellent mechanical properties and corrosion resistance prepared by mechanical alloying and hot pressing sintering, Mater. Des. 117 (2017) 193–202, https://doi.org/10.1016/j.matdes.2016.12.076.
[8] J. Ding, A. Inoue, Y. Han, F.L. Kong, S.L. Zhu, Z. Wang, E. Shalaan, F. Al-Marzouki, High entropy effect on structure and properties of (Fe,Co,Ni,Cr)-B amorphous alloys, J. Alloys Compd. 696 (2017) 345–352, https://doi.org/10.1016/j.jallcom.2016.11.223.
[9] Y. Zhang, T.T. Zuo, Z. Tang, M.C. Gao, K.A. Dahmen, P.K. Liaw, Z.P. Lu, Microstructures and properties of high-entropy alloys, Prog. Mater. Sci. 61 (2014) 1–93, https://doi.org/10.1016/j.pmatsci.2013.10.001.
[10] J.-W. Yeh, S.-K. Chen, S.-J. Lin, J.-Y. Gan, T. Chin, T.-T. Shun, C. Tsau, S.-Y. Chang, Nanostructured high-entropy alloys with multiple principal elements: novel alloy design concepts and outcomes, Adv. Eng. Mater. 6 (2004) 299–303, https://doi.org/10.1002/adem.200300567.
[11] B. Cantor, I.T.H. Chang, P. Knight, A.J.B. Vincent, Microstructural development in equiatomic multicomponent alloys, Mater. Sci. Eng., A 375–377 (2004) 213–218, https://doi.org/10.1016/j.msea.2003.10.257.
[12] J. Pang, H. Zhang, L. Zhang, Z. Zhu, H. Fu, H. Li, A. Wang, Z. Li, H. Zhang, Ductile Ti1.5ZrNbAl0.3 refractory high entropy alloy with high specific strength, Mater. Lett. 290 (2021), 129428, https://doi.org/10.1016/j.matlet.2021.129428.
[13] Y. Zhang, T. Ting, Z. Tang, M.C. Gao, K.A. Dahmen, P.K. Liaw, Z. Ping, Progress in materials science microstructures and properties of high-entropy alloys, Prog. Mater. Sci. 61 (2014) 1–93, https://doi.org/10.1016/j.pmatsci.2013.10.001.
[14] B. Schuh, F. Mendez-martin, B. Völker, E.P. George, H. Clemens, R. Pippan, A. Hohenwarter, Acta Materialia Mechanical properties , microstructure and thermal stability of a nanocrystalline CoCrFeMnNi high-entropy alloy after severe plastic deformation, Acta Mater. 96 (2015) 258–268, https://doi.org/10.1016/j.actamat.2015.06.025.
[15] B. Gludovatz, A. Hohenwarter, D. Catoor, E.H. Chang, E.P. George, R.O. Ritchie, A fracture-resistant high-entropy alloy for cryogenic applications, Science 345 (2014) 1153–1158, https://doi.org/10.1126/science.1254581.
[16] M.J. Yao, K.G. Pradeep, C.C. Tasan, D. Raabe, A novel, single phase, non-equiatomic FeMnNiCoCr high-entropy alloy with exceptional phase stability and tensile ductility, Scripta Mater. (2014) 72–73, https://doi.org/10.1016/j.scriptamat.2013.09.030, 5–8.
[17] Y. Deng, C.C. Tasan, K.G. Pradeep, H. Springer, A. Kostka, D. Raabe, Design of a twinning-induced plasticity high entropy alloy, Acta Mater. 94 (2015) 124–133, https://doi.org/10.1016/j.actamat.2015.04.014.
[18] M.A. Hemphill, T. Yuan, G.Y. Wang, J.W. Yeh, C.W. Tsai, A. Chuang, P.K. Liaw, Fatigue behavior of Al0.5CoCrCuFeNi high entropy alloys, Acta Mater. 60 (2012) 5723–5734, https://doi.org/10.1016/j.actamat.2012.06.046.
[19] C. Tong, Y. Chen, S. Chen, J. Yeh, T. Shun, C. Tsau, S. Lin, S. Chang, Microstructure Characterization of Al x CoCrCuFeNi High-Entropy Alloy System with Multiprincipal Elements, 2005, p. 36.
[20] B. Cantor, Multicomponent high-entropy Cantor alloys, Prog. Mater. Sci. 120 (2021), 100754, https://doi.org/10.1016/j.pmatsci.2020.100754.
[21] W. Li, D. Xie, D. Li, Y. Zhang, Y. Gao, P.K. Liaw, Mechanical behavior of high-entropy alloys, Prog. Mater. Sci. 118 (2021), 100777, https://doi.org/10.1016/j.pmatsci.2021.100777.
[22] Y. Lu, Y. Dong, S. Guo, L. Jiang, H. Kang, T. Wang, B. Wen, Z. Wang, J. Jie, Z. Cao, H. Ruan, T. Li, A promising new class of high-temperature alloys: eutectic high-entropy alloys, Sci. Rep. 4 (2015) 6200, https://doi.org/10.1038/srep06200.
[23] X. Jin, Y. Zhou, L. Zhang, X. Du, B. Li, A novel Fe 20 Co 20 Ni 41 Al 19 eutectic high entropy alloy with excellent tensile properties, Mater. Lett. 216 (2018) 144–146, https://doi.org/10.1016/j.matlet.2018.01.017.
[24] Y. Guo, L. Liu, Y. Zhang, J. Qi, B. Wang, Z. Zhao, J. Shang, J. Xiang, A superfine eutectic microstructure and the mechanical properties of CoCrFeNiMo x high-entropy alloys, J. Mater. Res. 33 (2018) 3258–3265, https://doi.org/10.1557/jmr.2018.177.
[25] Ł. Rogal, J. Morgiel, Z. Ś, F. Czerwi, Materials Science & Engineering A Microstructure and Mechanical Properties of the New Nb25Sc25Ti25Zr25 Eutectic High Entropy Alloy, vol. 651, 2016, pp. 590–597, https://doi.org/10.1016/j.msea.2015.10.071.
[26] P. Shi, W. Ren, T. Zheng, Z. Ren, X. Hou, J. Peng, P. Hu, Y. Gao, Y. Zhong, P. K. Liaw, Enhanced strength–ductility synergy in ultrafine-grained eutectic high-entropy alloys by inheriting microstructural lamellae, Nat. Commun. 10 (2019) 489, https://doi.org/10.1038/s41467-019-08460-2.
[27] I.S. Wani, T. Bhattacharjee, S. Sheikh, Y. Lu, S. Chatterjee, S. Guo, P. P. Bhattacharjee, N. Tsuji, Effect of severe cold-rolling and annealing on microstructure and mechanical properties of AlCoCrFeNi 2.1 eutectic high entropy alloy, IOP Conf. Ser. Mater. Sci. Eng. 194 (2017), 012018, https://doi.org/10.1088/1757-899X/194/1/012018.
[28] S.R. Reddy, S. Yoshida, T. Bhattacharjee, N. Sake, A. Lozinko, S. Guo, P. P. Bhattacharjee, N. Tsuji, Nanostructuring with structural-compositional dual heterogeneities enhances strength-ductility synergy in eutectic high entropy alloy, Sci. Rep. 9 (2019) 1–9, https://doi.org/10.1038/s41598-019-47983-y.
[29] T. Bhattacharjee, I.S. Wani, S. Sheikh, I.T. Clark, T. Okawa, S. Guo, P. P. Bhattacharjee, N. Tsuji, Simultaneous strength-ductility enhancement of a nano-lamellar AlCoCrFeNi2.1 eutectic high entropy alloy by cryo-rolling and annealing, Sci. Rep. 8 (2018) 3276, https://doi.org/10.1038/s41598-018-21385-y.
[30] M.H. Asoushe, A.Z. Hanzaki, H.R. Abedi, B. Mirshekari, T. Wegener, S.V. Sajadifar, T. Niendorf, Thermal stability, microstructure and texture evolution of thermomechanical processed AlCoCrFeNi2.1 eutectic high entropy alloy, Mater. Sci. Eng., A 799 (2021), 140012, https://doi.org/10.1016/j.msea.2020.140012.
[31] A. Patel, I. Wani, S.R. Reddy, S. Narayanaswamy, A. Lozinko, R. Saha, S. Guo, P. P. Bhattacharjee, Strain-path controlled microstructure, texture and hardness evolution in cryo-deformed AlCoCrFeNi 2.1 eutectic high entropy alloy, Intermetallics 97 (2018) 12–21, https://doi.org/10.1016/j.intermet.2018.03.007.
[32] T. Xiong, W. Yang, S. Zheng, Z. Liu, Y. Lu, R. Zhang, Y. Zhou, X. Shao, B. Zhang, J. Wang, F. Yin, P.K. Liaw, X. Ma, Faceted Kurdjumov-Sachs interface-induced slip continuity in the eutectic high-entropy alloy, AlCoCrFeNi2.1, J. Mater. Sci. Technol. 65 (2021) 216–227, https://doi.org/10.1016/j.jmst.2020.04.073.
[33] P. Shi, Y. Zhong, Y. Li, W. Ren, T. Zheng, Z. Shen, B. Yang, J. Peng, P. Hu, Y. Zhang, P.K. Liaw, Y. Zhu, Multistage work hardening assisted by multi-type twinning in ultrafine-grained heterostructural eutectic high-entropy alloys, Mater. Today 41 (2020) 62–71, https://doi.org/10.1016/j.mattod.2020.09.029.
[34] T. Bhattacharjee, R. Zheng, Y. Chong, S. Sheikh, S. Guo, I.T. Clark, T. Okawa, I. S. Wani, P.P. Bhattacharjee, A. Shibata, N. Tsuji, Effect of low temperature on tensile properties of AlCoCrFeNi2.1 eutectic high entropy alloy, Mater. Chem. Phys. 210 (2018) 207–212, https://doi.org/10.1016/j.matchemphys.2017.06.023.
[35] Y. Zhang, X. Wang, J. Li, Y. Huang, Y. Lu, X. Sun, Materials Science & Engineering A Deformation mechanism during high-temperature tensile test in an eutectic, Mater. Sci. Eng., A 724 (2018) 148–155, https://doi.org/10.1016/j.msea.2018.03.078.
[36] S. Shukla, T. Wang, S. Cotton, R.S. Mishra, Hierarchical microstructure for improved fatigue properties in a eutectic high entropy alloy, Scripta Mater. 156 (2018) 105–109, https://doi.org/10.1016/j.scriptamat.2018.07.022.
[37] N.R. Jaladurgam, A. Lozinko, S. Guo, T.L. Lee, M. Hörnqvist Colliander, Temperature dependent load partitioning and slip mode transition in a eutectic AlCoCrFeNi2.1 high entropy alloy, Materialia 17 (2021), 101118, https://doi.org/10.1016/j.mtla.2021.101118.
[38] L. Wang, C. Yao, J. Shen, Y. Zhang, T. Wang, Y. Ge, L. Gao, G. Zhang, Microstructures and room temperature tensile properties of as-cast and directionally solidified AlCoCrFeNi2.1 eutectic high-entropy alloy, Intermetallics 118 (2020), 106681, https://doi.org/10.1016/j.intermet.2019.106681.
[39] Y. Zhang, X. Wang, J. Li, Y. Huang, Y. Lu, X. Sun, Deformation mechanism during high-temperature tensile test in an eutectic high-entropy alloy AlCoCrFeNi2.1, Mater. Sci. Eng., A 724 (2018) 148–155, https://doi.org/10.1016/j.msea.2018.03.078.
[40] T.S. Reddy, I.S. Wani, T. Bhattacharjee, S.R. Reddy, R. Saha, P.P. Bhattacharjee, Severe plastic deformation driven nanostructure and phase evolution in a Al0.5CoCrFeMnNi dual phase high entropy alloy, Intermetallics 91 (2017) 150–157, https://doi.org/10.1016/j.intermet.2017.09.002.
[41] I.S. Wani, T. Bhattacharjee, S. Sheikh, P.P. Bhattacharjee, S. Guo, N. Tsuji, Tailoring nanostructures and mechanical properties of AlCoCrFeNi2.1 eutectic high entropy alloy using thermo-mechanical processing, Mater. Sci. Eng., A 675 (2016) 99–109, https://doi.org/10.1016/j.msea.2016.08.048.
[42] Y. Lu, X. Gao, L. Jiang, Z. Chen, T. Wang, Acta Materialia Directly cast bulk eutectic and near-eutectic high entropy alloys with balanced strength and ductility in a wide temperature range, Acta Mater. 124 (2017) 143–150, https://doi.org/10.1016/j.actamat.2016.11.016.
[43] P. Li, H. Sun, S. Wang, X. Hao, H. Dong, Rotary friction welding of AlCoCrFeNi2.1 eutectic high entropy alloy, J. Alloys Compd. 814 (2020), 152322, https://doi.org/10.1016/j.jallcom.2019.152322.
[44] P. Li, S. Wang, Y. Xia, X. Hao, H. Dong, Diffusion bonding of AlCoCrFeNi2.1 eutectic high entropy alloy to TiAl alloy, J. Mater. Sci. Technol. 45 (2020) 59–69, https://doi.org/10.1016/j.jmst.2019.10.041.
[45] L. Zhang, Y. Zhang, Tensile properties and impact toughness of AlCoxCrFeNi3.1–x (x = 0.4, 1) high-entropy alloys, Frontiers in Materials 7 (2020), https://doi.org/10.3389/fmats.2020.00092.
[46] D. Choudhuri, S.G. Srinivasan, R.S. Mishra, Deformation of lamellar FCC-B2 nanostructures containing Kurdjumov-Sachs interfaces: relation between interfacial structure and plasticity, Int. J. Plast. 125 (2020) 191–209, https://doi.org/10.1016/j.ijplas.2019.09.014.
[47] Y. Zhang, J. Li, X. Wang, Y. Lu, Y. Zhou, X. Sun, The interaction and migration of deformation twin in an eutectic high-entropy alloy AlCoCrFeNi2.1, J. Mater. Sci. Technol. 35 (2019) 902–906, https://doi.org/10.1016/j.jmst.2018.09.067.

[48] J. Miao, H. Liang, A. Zhang, J. He, J. Meng, Y. Lu, Tribological behavior of an AlCoCrFeNi2.1 eutectic high entropy alloy sliding against different counterfaces, Tribol. Int. 153 (2021), 106599, https://doi.org/10.1016/j.triboint.2020.106599.
[49] S.R. Reddy, U. Sunkari, A. Lozinko, R. Saha, S. Guo, P.P. Bhattacharjee, Microstructural design by severe warm-rolling for tuning mechanical properties of AlCoCrFeNi2.1 eutectic high entropy alloy, Intermetallics 114 (2019), https://doi.org/10.1016/j.intermet.2019.106601.
[50] T. Wang, M. Komarasamy, S. Shukla, R.S. Mishra, Simultaneous enhancement of strength and ductility in an AlCoCrFeNi2.1 eutectic high-entropy alloy via friction stir processing, J. Alloys Compd. 766 (2018) 312–317, https://doi.org/10.1016/j.jallcom.2018.06.337.
[51] W. Zhang, L. Liu, S. Peng, J. Ren, F. Wu, J. Shang, M. Chen, Y. Zhang, Z. Zhao, J. Qi, B. Wang, W. Chen, The tensile property and notch sensitivity of AlCoCrFeNi2.1 high entropy alloy with a novel "steel-frame" eutectic microstructure, J. Alloys Compd. 863 (2021), 158747, https://doi.org/10.1016/j.jallcom.2021.158747.
[52] S.R. Reddy, U. Sunkari, A. Lozinko, S. Guo, P.P. Bhattacharjee, Development and homogeneity of microstructure and texture in a lamellar AlCoCrFeNi 2.1 eutectic high-entropy alloy severely strained in the warm-deformation regime, J. Mater. Res. 34 (2019) 687–699, https://doi.org/10.1557/jmr.2018.409.
[53] D. Choudhuri, S. Shukla, P.A. Jannotti, S. Muskeri, S. Mukherjee, J.T. Lloyd, R. S. Mishra, Characterization of as-cast microstructural heterogeneities and damage mechanisms in eutectic AlCoCrFeNi2.1 high entropy alloy, Mater. Char. 158 (2019), 109955, https://doi.org/10.1016/j.matchar.2019.109955.
[54] Y. Lu, X. Gao, L. Jiang, Z. Chen, T. Wang, J. Jie, H. Kang, Y. Zhang, S. Guo, H. Ruan, Y. Zhao, Z. Cao, T. Li, Directly cast bulk eutectic and near-eutectic high entropy alloys with balanced strength and ductility in a wide temperature range, Acta Mater. 124 (2017) 143–150, https://doi.org/10.1016/j.actamat.2016.11.016.
[55] W. Chen, Y. Wang, L. Wang, J. Zhou, Effect of lamellar microstructure on fatigue crack initiation and propagation in AlCoCrFeNi2.1 eutectic high-entropy alloy, Eng. Fract. Mech. 246 (2021), 107615, https://doi.org/10.1016/j.engfracmech.2021.107615.
[56] A.P. Hammersley, S.O. Svensson, M. Hanfland, A.N. Fitch, D. Hausermann, Two-dimensional detector software: from real detector to idealised image or two-theta scan, High Pres. Res. 14 (1996) 235–248, https://doi.org/10.1080/08957959608201408.
[57] A.P. Hammersley, S.O. Svensson, A. Thompson, Calibration and correction of spatial distortions in 2D detector systems, Nucl. Instrum. Methods Phys. Res. Sect. A Accel. Spectrom. Detect. Assoc. Equip. 346 (1994) 312–321, https://doi.org/10.1016/0168-9002(94)90720-X.
[58] B.H. Toby, R.B. Von Dreele, GSAS-II : the genesis of a modern open-source all purpose crystallography software package, J. Appl. Crystallogr. 46 (2013) 544–549, https://doi.org/10.1107/S0021889813003531.
[59] H.-R. Wenk, L. Lutterotti, P. Kaercher, W. Kanitpanyacharoen, L. Miyagi, R. Vasin, Rietveld texture analysis from synchrotron diffraction images. II. Complex multiphase materials and diamond anvil cell experiments, Powder Diffr. 29 (2014) 220–232, https://doi.org/10.1017/S0885715614000360.
[60] L. Lutterotti, R. Vasin, H.-R. Wenk, Rietveld texture analysis from synchrotron diffraction images. I. Calibration and basic analysis, Powder Diffr. 29 (2014) 76–84, https://doi.org/10.1017/S0885715613001346.
[61] P. Barriobero-Vila, R. Jerez-Mesa, A. Guitar, O. Gavalda-Diaz, J.A. Travieso-Rodríguez, A. Stark, N. Schell, J. Llumà, G. Fargas, A. Mateo, J.J. Roa, Deformation kinetics of a TRIP steel determined by in situ high-energy synchrotron X-ray diffraction, Materialia 20 (2021), 101251, https://doi.org/10.1016/j.mtla.2021.101251.
[62] N.C. Popa, The (hkl) dependence of diffraction-line broadening caused by strain and size for all laue groups in Rietveld refinement, J. Appl. Crystallogr. 31 (1998) 176–180, https://doi.org/10.1107/S0021889897009795.
[63] L. Lutterotti, D. Chateigner, S. Ferrari, J. Ricote, Texture, residual stress and structural analysis of thin films using a combined X-ray analysis, Thin Solid Films 450 (2004) 34–41, https://doi.org/10.1016/j.tsf.2003.10.150.
[64] F. Lin, N. Hilairet, P. Raterron, A. Addad, J. Immoor, H. Marquardt, C.N. Tomé, L. Miyagi, S. Merkel, Elasto-viscoplastic self consistent modeling of the ambient temperature plastic behavior of periclase deformed up to 5.4 GPa, J. Appl. Phys. 122 (2017), 205902, https://doi.org/10.1063/1.4999951.
[65] J. Shen, Z. Zeng, M. Nematollahi, N. Schell, E. Maawad, R.N. Vasin, K. Safaei, B. Poorganji, M. Elahinia, J.P. Oliveira, In-situ synchrotron X-ray diffraction analysis of the elastic behaviour of martensite and H-phase in a NiTiHf high temperature shape memory alloy fabricated by laser powder bed fusion, Additive Manufacturing Letters 1 (2021), 100003, https://doi.org/10.1016/j.addlet.2021.100003.
[66] Y. Wang, B. Liu, K. Yan, M. Wang, S. Kabra, Y.-L. Chiu, D. Dye, P.D. Lee, Y. Liu, B. Cai, Probing deformation mechanisms of a FeCoCrNi high-entropy alloy at 293 and 77 K using in situ neutron diffraction, Acta Mater. 154 (2018) 79–89, https://doi.org/10.1016/j.actamat.2018.05.013.
[67] Y. Shi, S. Li, T.L. Lee, X. Hui, Z. Zhang, R. Li, M. Zhang, S. Kabra, Y.-D. Wang, In situ neutron diffraction study of a new type of stress-induced confined martensitic transformation in Fe22Co20Ni19Cr20Mn12Al7 high-entropy alloy, Mater. Sci. Eng., A 771 (2020), 138555, https://doi.org/10.1016/j.msea.2019.138555.
[68] P. Shi, R. Li, Y. Li, Y. Wen, Y. Zhong, W. Ren, Z. Shen, T. Zheng, J. Peng, X. Liang, P. Hu, N. Min, Y. Zhang, Y. Ren, P.K. Liaw, D. Raabe, Y.-D. Wang, Hierarchical crack buffering triples ductility in eutectic herringbone high-entropy alloys, Science 373 (2021) 912–918, https://doi.org/10.1126/science.abf6986.
[69] L. Ma, L. Wang, Z. Nie, F. Wang, Y. Xue, J. Zhou, T. Cao, Y. Wang, Y. Ren, Reversible deformation-induced martensitic transformation in Al0.6CoCrFeNi high-entropy alloy investigated by in situ synchrotron-based high-energy X-ray diffraction, Acta Mater. 128 (2017) 12–21, https://doi.org/10.1016/j.actamat.2017.02.014.
[70] N. Jia, Z.H. Cong, X. Sun, S. Cheng, Z.H. Nie, Y. Ren, P.K. Liaw, Y.D. Wang, An in situ high-energy X-ray diffraction study of micromechanical behavior of multiple phases in advanced high-strength steels, Acta Mater. 57 (2009) 3965–3977, https://doi.org/10.1016/j.actamat.2009.05.002.
[71] M. Zhang, H. Chen, Y. Wang, S. Wang, R. Li, S. Li, Y.-D. Wang, Deformation-induced martensitic transformation kinetics and correlative micromechanical behavior of medium-Mn transformation-induced plasticity steel, J. Mater. Sci. Technol. 35 (2019) 1779–1786, https://doi.org/10.1016/j.jmst.2019.04.007.
[72] A.M. Korsunsky, S.P. Collins, R.A. Owen, M.R. Daymond, S. Achtioui, K.E. James, Fast residual stress mapping using energy-dispersive synchrotron X-ray diffraction on station 16.3 at the SRS, J. Synchrotron Radiat. 9 (2002) 77–81, https://doi.org/10.1107/S0909049502001905.
[73] C. Zheng, Q. Zhen, Y. Wang, N. Li, Low temperature macro- and micro-mechanical behavior of an ultrafine-grained metastable 304 austenitic stainless steel investigated by in situ high-energy X-ray diffraction, Mater. Sci. Eng., A 817 (2021), 141295, https://doi.org/10.1016/j.msea.2021.141295.
[74] B. Peng, J. Jie, J. Liu, J. Qu, M. Wang, J. Sun, X. Chen, Z. Ren, T. Li, Synergetic strengthening of heterogeneous interface far beyond rule of mixture in Cu/1010 steel bimetal laminar composite, Mater. Sci. Eng., A 851 (2022), 143609, https://doi.org/10.1016/j.msea.2022.143609.
[75] N.R. Jaladurgam, A. Lozinko, S. Guo, T.L. Lee, M. Hörnqvist Colliander, Temperature dependent load partitioning and slip mode transition in a eutectic AlCoCrFeNi2.1 high entropy alloy, Materialia 17 (2021), 101118, https://doi.org/10.1016/j.mtla.2021.101118.
[76] G.K. Williamsont, W.H. Hallt, X-Ray Line Broadening from Filed Aluminium and Wolfram, (n.d)..
[77] A. Khorsand Zak, W.H. Abd Majid, M.E. Abrishami, R. Yousefi, X-ray analysis of ZnO nanoparticles by Williamson-Hall and size-strain plot methods, Solid State Sci. 13 (2011) 251–256, https://doi.org/10.1016/j.solidstatesciences.2010.11.024.
[78] A. Scheer, H. Kruppke, R. Heib, Diffraction Analysis of the Microstructure of Materials, Springer-Verlag Berlin Heidelberg GmbH, 2001. http://download.springer.com/static/pdf/185/bfm%253A978-3-642-56668-4%252F1.pdf?auth66=1401995374_4d363c462609ae19e3de18b0ee51ef07&ext=.pdf.
[79] H. Cheng, H.Y. Wang, Y.C. Xie, Q.H. Tang, P.Q. Dai, Controllable fabrication of a carbide-containing FeCoCrNiMn high-entropy alloy: microstructure and mechanical properties, Mater. Sci. Technol. 33 (2017) 2032–2039, https://doi.org/10.1080/02670836.2017.1342367.
[80] J.Y. He, H. Wang, H.L. Huang, X.D. Xu, M.W. Chen, Y. Wu, X.J. Liu, T.G. Nieh, K. An, Z.P. Lu, A precipitation-hardened high-entropy alloy with outstanding tensile properties, Acta Mater. 102 (2016) 187–196, https://doi.org/10.1016/j.actamat.2015.08.076.
[81] H. Adachi, Y. Karamatsu, S. Nakayama, T. Miyazawa, M. Sato, T. Yamasaki, Elastic and plastic deformation behavior studied by *in-situ* synchrotron X-ray diffraction in nanocrystalline nickel, Mater. Trans. 57 (2016) 1447–1453, https://doi.org/10.2320/matertrans.MH201505.
[82] Y. Miyajima, S. Okubo, T. Miyazawa, H. Adachi, T. Fujii, In-situ X-ray diffraction during tensile deformation of ultrafine-grained copper using synchrotron radiation, Phil. Mag. Lett. 96 (2016) 294–304, https://doi.org/10.1080/09500839.2016.1218563.
[83] J. Joseph, N. Stanford, P. Hodgson, D.M. Fabijanic, Understanding the mechanical behaviour and the large strength/ductility differences between FCC and BCC AlxCoCrFeNi high entropy alloys, J. Alloys Compd. 726 (2017) 885–895, https://doi.org/10.1016/j.jallcom.2017.08.067.
[84] H.Y. Yasuda, K. Shigeno, T. Nagase, Dynamic strain aging of Al 0.3 CoCrFeNi high entropy alloy single crystals, Scripta Mater. 108 (2015) 80–83, https://doi.org/10.1016/j.scriptamat.2015.06.022.
[85] S. Il Baik, S.Y. Wang, P.K. Liaw, D.C. Dunand, Increasing the creep resistance of Fe-Ni-Al-Cr superalloys via Ti additions by optimizing the B2/L21 ratio in composite nano-precipitates, Acta Mater. 157 (2018) 142–154, https://doi.org/10.1016/j.actamat.2018.07.025.
[86] T. Xiong, S. Zheng, J. Pang, X. Ma, High-strength and high-ductility AlCoCrFeNi2.1 eutectic high-entropy alloy achieved via precipitation strengthening in a heterogeneous structure, Scripta Mater. 186 (2020) 336–340, https://doi.org/10.1016/j.scriptamat.2020.04.035.
[87] T. Xiong, W. Yang, S. Zheng, Z. Liu, Y. Lu, R. Zhang, Y. Zhou, X. Shao, B. Zhang, J. Wang, F. Yin, P.K. Liaw, X. Ma, Journal of materials science & technology faceted kurdjumov-sachs interface-induced slip continuity in the, J. Mater. Sci. Technol. 65 (2021) 216–227, https://doi.org/10.1016/j.jmst.2020.04.073.
[88] R.J. Vikram, B.S. Murty, D. Fabijanic, S. Suwas, Insights into micro-mechanical response and texture of the additively manufactured eutectic high entropy alloy AlCoCrFeNi2.1, J. Alloys Compd. 827 (2020), 154034, https://doi.org/10.1016/j.jallcom.2020.154034.
[89] X. Gao, Y. Lu, B. Zhang, N. Liang, G. Wu, G. Sha, J. Liu, Y. Zhao, Microstructural origins of high strength and high ductility in an AlCoCrFeNi2.1 eutectic high-entropy alloy, Acta Mater. 141 (2017) 59–66, https://doi.org/10.1016/j.actamat.2017.07.041.
[90] S. Muskeri, V. Hasannaeimi, R. Salloom, M. Sadeghilaridjani, S. Mukherjee, Small-scale mechanical behavior of a eutectic high entropy alloy, Sci. Rep. 10 (2020), https://doi.org/10.1038/s41598-020-59513-2.
[91] N. Park, B.-J. Lee, N. Tsuji, The phase stability of equiatomic CoCrFeMnNi high-entropy alloy: comparison between experiment and calculation results, J. Alloys Compd. 719 (2017) 189–193, https://doi.org/10.1016/j.jallcom.2017.05.175.
[92] Y.C. Liang, J.T. Guo, Y. Xie, L.Y. Sheng, L.Z. Zhou, Z.Q. Hu, Effect of growth rate on the tensile properties of DS NiAl/Cr(Mo) eutectic alloy produced by liquid metal

cooling technique, Intermetallics 18 (2010) 319–323, https://doi.org/10.1016/j.intermet.2009.08.002.
[93] K. Yamanaka, M. Mori, K. Kuramoto, A. Chiba, Development of new Co–Cr–W-based biomedical alloys: effects of microalloying and thermomechanical processing on microstructures and mechanical properties, Mater. Des. 55 (2014) 987–998, https://doi.org/10.1016/j.matdes.2013.10.052.
[94] B. Wang, H. He, M. Naeem, S. Lan, S. Harjo, T. Kawasaki, Y. Nie, H.W. Kui, T. Ungár, D. Ma, A.D. Stoica, Q. Li, Y. Ke, C.T. Liu, X.-L. Wang, Deformation of CoCrFeNi high entropy alloy at large strain, Scripta Mater. 155 (2018) 54–57, https://doi.org/10.1016/j.scriptamat.2018.06.013.
[95] N. Stepanov, M. Tikhonovsky, N. Yurchenko, D. Zyabkin, M. Klimova, S. Zherebtsov, A. Efimov, G. Salishchev, Effect of cryo-deformation on structure and properties of CoCrFeNiMn high-entropy alloy, Intermetallics 59 (2015) 8–17, https://doi.org/10.1016/j.intermet.2014.12.004.
[96] S. Morooka, Y. Tomota, T. Kamiyama, Heterogeneous deformation behavior studied by in situ neutron diffraction during tensile deformation for ferrite, martensite and pearlite steels, ISIJ Int. 48 (2008) 525–530, https://doi.org/10.2355/isijinternational.48.525.
[97] Y. Tomota, P. Lukáš, D. Neov, S. Harjo, Y.R. Abe, In situ neutron diffraction during tensile deformation of a ferrite-cementite steel, Acta Mater. 51 (2003) 805–817, https://doi.org/10.1016/S1359-6454(02)00472-X.
[98] Y. Tomota, P. Lukas, S. Harjo, J.H. Park, N. Tsuchida, D. Neov, In situ neutron diffraction study of IF and ultra low carbon steels upon tensile deformation, Acta Mater. 51 (2003) 819–830, https://doi.org/10.1016/S1359-6454(02)00473-1.
[99] K. Ma, H. Wen, T. Hu, T.D. Topping, D. Isheim, D.N. Seidman, E.J. Lavernia, J. M. Schoenung, Mechanical behavior and strengthening mechanisms in ultrafine grain precipitation-strengthened aluminum alloy, Acta Mater. 62 (2014) 141–155, https://doi.org/10.1016/j.actamat.2013.09.042.